scientific reports

Check for updates

OPEN

# Hybrid classical and quantum computing for enhanced glioma tumor classification using TCGA data

Emine Akpinar✉ & Murat Oduncuoglu

**Gliomas are the most prevalent malignant primary brain tumors and present diagnostic challenges due to varying survival rates and treatment responses between low-grade gliomas (LGGs) and high-grade gliomas (HGGs). Accurate classification is crucial for effective treatment and prognosis. While classical AI methods have shown promise in glioma classification, the growing volume of medical data, inherent noise, and limitations of classical vector spaces present significant challenges. However, quantum computing-based AI methods have the potential to process data in parallel by leveraging quantum properties such as superposition and entanglement, analyze higher-dimensional data more efficiently, and solve certain problems that classical methods struggle with more rapidly and effectively. This study introduces a novel hybrid classical and quantum computing model to distinguish LGGs from HGGs using data from The Cancer Genome Atlas (TCGA). In the classical part, an ensemble feature selection method was employed to identify the most informative molecular markers and clinical features in the TCGA. In the quantum component, six variational quantum classifier (VQC) models with varying hyperparameters were evaluated. These classifiers utilize selected features to differentiate LGGs from HGGs. Among these, the VQC-1 model, which employs $R_x$ and CX gates in the feature map and $R_y$, $R_z$ and CY gates in the parameterized quantum circuit, achieved the highest classification accuracy of 0.74 using the AQCD optimization method. Additionally, VQC-1 identified IDH1, age at diagnosis, PTEN, EGFR, and ATRX, in descending order of importance, as the most informative features distinguishing LGGs from HGGs. Compared to classical machine learning models, VQC-1 demonstrated performance comparable to that of XGBoost and GBM, while outperformed KNN, SVC, DTC, and RFC in five-fold cross-validation experiments. This study provides a novel perspective on glioma classification by integrating classical and quantum computing, offering valuable insights into hybrid computational approaches.**

**Keywords** Hybrid classical and quantum computing, Glioma, Variational quantum classifier, Ensemble feature selection, Molecular markers

Exploring the intricate landscape of brain tumors reveals challenges that are both formidable and intriguing within the realm of human health. As one navigates this complex terrain, glioma tumors emerge as a focal point, encapsulating not only the urgency of clinical intervention but also the depth of scientific fascination. Gliomas or glioma tumors arise from glial cells and are the most common cancer of the central nervous system (CNS), accounting for approximately 80% of all malignant primary brain and CNS tumors[1–3]. Following the World Health Organization (WHO) classification of CNS tumors, gliomas can be broadly categorized into two groups: low-grade gliomas (LGGs, WHO grades II and III) and high-grade gliomas (HGGs, WHO grade IV) including glioblastoma multiforme (GBM)[4]. LGGs are invasive tumors that commonly develop in the cerebral hemispheres of adults and include astrocytomas, oligodendrogliomas, and oligoastrocytomas, and survival for patients with LGGs ranges widely from 1 to 15 years[5]. Some subsets of LGGs can evolve into GBM within a few months, whereas others may maintain stability for several years[6]. GBM is the most common and most aggressive type of glioma, accounting for more than 50% of all gliomas and is the most common malignant primary brain tumor[7–9]. GBM is a relatively uncommon tumor with a global incidence rate of only 3.17 per 100,000 people; however, GBM has a profound impact on patients' lives due to its grim prognosis, with a median survival of only 12–15 months from diagnosis[10,11]. The treatment modality for gliomas is a multidisciplinary approach

Department of Physics, Yildiz Technical University, Istanbul, Turkey. ✉email: emineakpinar28@gmail.com

that generally consists of surgery, radiotherapy, and chemotherapy[12]. However, given that LGGs and HGGs are known to exhibit different responses to treatments and have distinct prognoses, accurate and early diagnosis, classification, and grading are critical for making appropriate treatment decisions[13–15].

With reference to the fourth edition of the WHO Classification of Tumors of the CNS released in 2016, gliomas are classified from Grade II to Grade IV by not only histological characteristics but also several molecular features (or molecular markers/biomarkers), such as IDH (IDH1 and IDH2, briefly IDH) mutation, TP53 and ATRX, and chromosome 1p/19q codeletion status[16]. For instance, mutations in IDH characterize the majority of LGGs in adults and are associated with a more favorable prognosis than are mutations in nonmutated IDH[10,17–19]. Additionally, TP53 and ATRX mutations are more commonly observed in astrocytomas and serve as significant markers of clinical behavior[20]. In addition, due to the rapid advances in the molecular level understanding of CNS tumors, the WHO made significant revisions to tumor classification in 2021, emphasizing the importance of molecular detection[21]. Recently, an enhanced understanding of the molecular determinants of glioma cell invasion has provided valuable insights into the fundamental biological characteristics of this disease. Genetic information about the tumor is necessary for the accurate monitoring of patients with gliomas and for the guidance of personalized therapies[22]. Ultimately, clinicians increasingly rely on and demand genetic classifications to better guide the clinical decision-making process. In the cancer research community, The Cancer Genome Atlas (TCGA) research project has been established to provide comprehensive analysis of various cancer genome profiles, such as gliomas[23]. To generate these genomic profiles, TCGA was generated with high-throughput technologies based on microarray and next-generation sequencing methods. Furthermore, for optimal patient management, clinical features such as age and gender have been included in combination with molecular markers, as they contribute to the tumor classification process[24,25].

Lately, while molecular markers and clinical characteristics have been extensively utilized to differentiate between glioma tumors, only a handful of these attributes provide dependable and consistently reproducible predictive indicators. In the absence of objective characteristics, the classification of glioma tumors becomes notably subjective and reliant on the personal biases of individual diagnosticians[26]. Moreover, molecular genetic testing can be costly or not easily accessible, and the process of obtaining results can take weeks, potentially causing delays in critical treatment decisions[18,27–29]. Consequently, numerous studies have underscored the importance of identifying significant and effective molecular markers and clinical features in conjunction with precise classification methods to increase the accuracy of glioma tumor classification. There has been a significant increase in interest in and application of various classical artificial intelligence (AI) methods, such as machine learning (ML) and deep learning (DL), in the field of glioma tumor research in recent years. These advanced AI approaches have found extensive utility in diverse aspects of glioma tumor analysis, including tumor grading and diagnosis[13,30–37], noninvasive identification of genomic biomarkers[38–42], and prediction of patient survival outcomes[43–46]. Previous studies have demonstrated the effectiveness of various AI techniques in distinguishing (and grading) LGGs from HGGs by using molecular markers such as IDH, TP53, and ATRX mutation status; the presence of 1p/19q codeletion; MGMT promoter methylation status; and other molecular attributes and clinical features[13,26].

On the other hand, classical AI approaches encounter constraints attributed to factors such as data quality and noise, feature dimensionality, intricate relationships among features, and the dimension of the classical vector space[47,48]. The diagnosis and treatment results are affected by these situations. Moreover, advanced classical AI methods require increased computational power as the amount of genomic and clinical data increases. Nevertheless, classical computers equipped with CPU and GPU face limitations in resolving certain complex health issues, such as early cancer diagnosis, tumor classification, simulation of molecular structures, and drug discovery[49,50]. This motivates the necessity of quantum computing and quantum computing-based AI techniques capable of generating solutions to the aforementioned problems, facilitating precise and detailed early disease discovery.

Quantum computing is a swiftly progressing domain within the realms of science and technology, harnessing the tenets of quantum mechanics to address challenges that surpass the capabilities of classical computers. Quantum computers possess parallel processing power due to the superposition and quantum entanglement properties inherent in quantum particles. Considering the vastness of the quantum Hilbert space, they offer several advantages, such as a wide information capacity and noise resistance, which are particularly beneficial for noisy medical data[49]. Among the various quantum algorithms proposed as solutions to medical challenges, quantum-enhanced AI/ML methods stand out for their broad applicability. Recently, quantum computing and quantum AI methods have been shown to have numerous applications in the field of healthcare, including rapid genome analysis and sequencing[51,52], disease detection[53–56], classification[57–61], identification of new drug applications[62–64]. Furthermore, quantum computing models play a significant role in predicting the mutations of genes that are particularly critical in the pathogenesis and diagnosis of specific cancer types, such as GBM[65].

However, despite the substantial promise inherent in quantum computing, current noisy intermediate-scale quantum (NISQ) computers have limited qubits and low circuit depths[66]. Furthermore, these computers are highly susceptible to their ambient surroundings and are at risk of losing their quantum state because of quantum decoherence[67]. Variational quantum algorithm/classifier (VQA/VQC) has emerged as promising approaches for exploiting quantum advantages in NISQ devices, and this algorithm has applications in various fields, such as universal quantum computing, dynamic quantum simulation, optimization and quantum ML[68–73]. VQC employs classical optimization methods to train parametrized quantum circuits, determining the optimal parameters for achieving quantum advantage on NISQ computers[71,74,75]. In addition, hybrid classical and quantum models, whose quantum component is VQC, have been successfully applied in solving problems in many medical fields, such as disease detection and classification[76–80]. These hybrid frameworks help explore the potential computational power of NISQ computers. In other words, hybrid models combine the speed and

parallel processing capabilities of quantum computing with the robustness and flexibility of classical computing, enabling greater practicality in real-world applications.

Existing methods in glioma classification suffer from significant limitations, including limited access to genetic tests, reliance on subjective interpretations, data-related issues, and computational bottlenecks in classical algorithms. These factors restrict the diagnostic accuracy and reliability of current approaches. To address these challenges, this study proposes a hybrid classical and quantum computing model that combines ensemble feature selection with VQCs. By integrating the strengths of both classical and quantum computing paradigms, this study aims to overcome the traditional limitations of classical models and achieve higher accuracy and efficiency in glioma classification, contributing to the generalizability of the hybrid classical and quantum computing model. As a result, this study seeks to contribute to the glioma classification problem by presenting a novel classification methodology developed through the synergy of classical and quantum computing paradigms.

The primary contributions of this research can be outlined as follows:

- To the best of our knowledge, this study is the first to utilize TCGA data within a hybrid classical and quantum computing system. The most informative molecular markers and clinical features determined through the ensemble feature selection method were employed within the VQC methods for distinguishing between LGGs and HGGs.
- By varying hyperparameters such as feature maps, parameterized quantum circuit structures, and optimization methods of VQCs, an optimal circuit design was achieved with minimum quantum gate usage and circuit depth. This resulted in VQC-1, which demonstrated the highest classification accuracy in differentiating LGGs from HGGs.
- The ability of the most informative molecular and clinical features, identified through the ensemble feature selection method, to distinguish LGGs from HGGs was re-evaluated using VQC-1 and ranked in descending order of importance.
- The most informative features determined through VQC-1 were subsequently compared with the results in the literature.
- The performance of the VQC-1 model is compared with six different classical ML algorithms and similar studies in the literature using the five-fold cross-validation method.
- To evaluate the performance of all the proposed VQCs, AUROC analysis was performed, and accuracy, precision, recall, and F1-score were calculated based on the confusion matrix.

The rest of this study is organized in the following manner:

In "Preliminaries", we delve into the background of quantum computation, introducing fundamental physical concepts related to quantum computation such as Dirac notation, quantum bits, quantum gates, and quantum circuits. "Methods" presents the classical and quantum computation methods employed in our study. While the classical computation section covers preprocessing, feature selection methods and the ensemble feature selection method, the quantum computation section provides detailed explanations of feature mapping, parametrized quantum circuit, optimization, and measurement within the VQC framework. In "Experimental work", we elaborate on the platform, dataset, and evaluation metrics used in our research. "Experimental results" sequentially addresses the ensemble feature selection method and presents the outputs of VQC models. A thorough examination of the classification performance of the key molecular markers and clinical features was conducted, and a correlation analysis was carried out between these features and the grade of glioma tumors. At the end of this section, the classification results of the classical ML algorithms are presented using five-fold cross-validation. Finally, in "Discussion", we discuss all the outputs outlined in "Experimental results", considering other studies in the literature, and we present the main findings obtained in our study. The flowchart of the proposed hybrid classical and quantum computing model, illustrating the key components and workflow including preprocessing steps, ensemble feature selection, VQC model training, performance evaluation, and the selection process of the most informative features, is shown in Fig. 1.

## Preliminaries

In this section, quantum computing and its associated concepts, such as Dirac notation, quantum bits, quantum gates, and quantum circuits, are briefly introduced.

### Quantum computing

Quantum computation represents an ambitious emerging domain wherein computer science, mathematics, and physics converge to advance computational technologies rooted in the principles of quantum mechanics. Moreover, quantum computing is centered on the examination of challenges related to the storage, manipulation, and transmission of data encoded within quantum mechanical systems. These operations effectively harness quantum mechanical phenomena such as superposition and entanglement[81]. At its most fundamental level, a qubit can exist in either the state $|0\rangle$ or the state $|1\rangle$ . Additionally, it has the capability to exist in linear combinations of these states, denoted as superposition states $|0\rangle$ and $|1\rangle$ , respectively. In other words, superposition refers to the ability of a qubit to exist in more than one state simultaneously. This feature endows quantum computers with the ability to perform multiple computations simultaneously, which is not possible in classical computers and is one of the most important characteristics of quantum computing. However, superposition is preserved as coherent states. When a quantum system undergoes interaction with the environment, superposition can be lost, and a decoherence situation occurs. The other of the most important and exciting topics in quantum mechanics is the property known as entanglement, also referred to as "spooky action at a distance," which is exhibited by particles. This phenomenon was demonstrated in the EPR (Einstein, Podolsky, Rosen) experiment. In light of this experiment, when two particles engage in interaction and subsequently part ways (such as particles A and

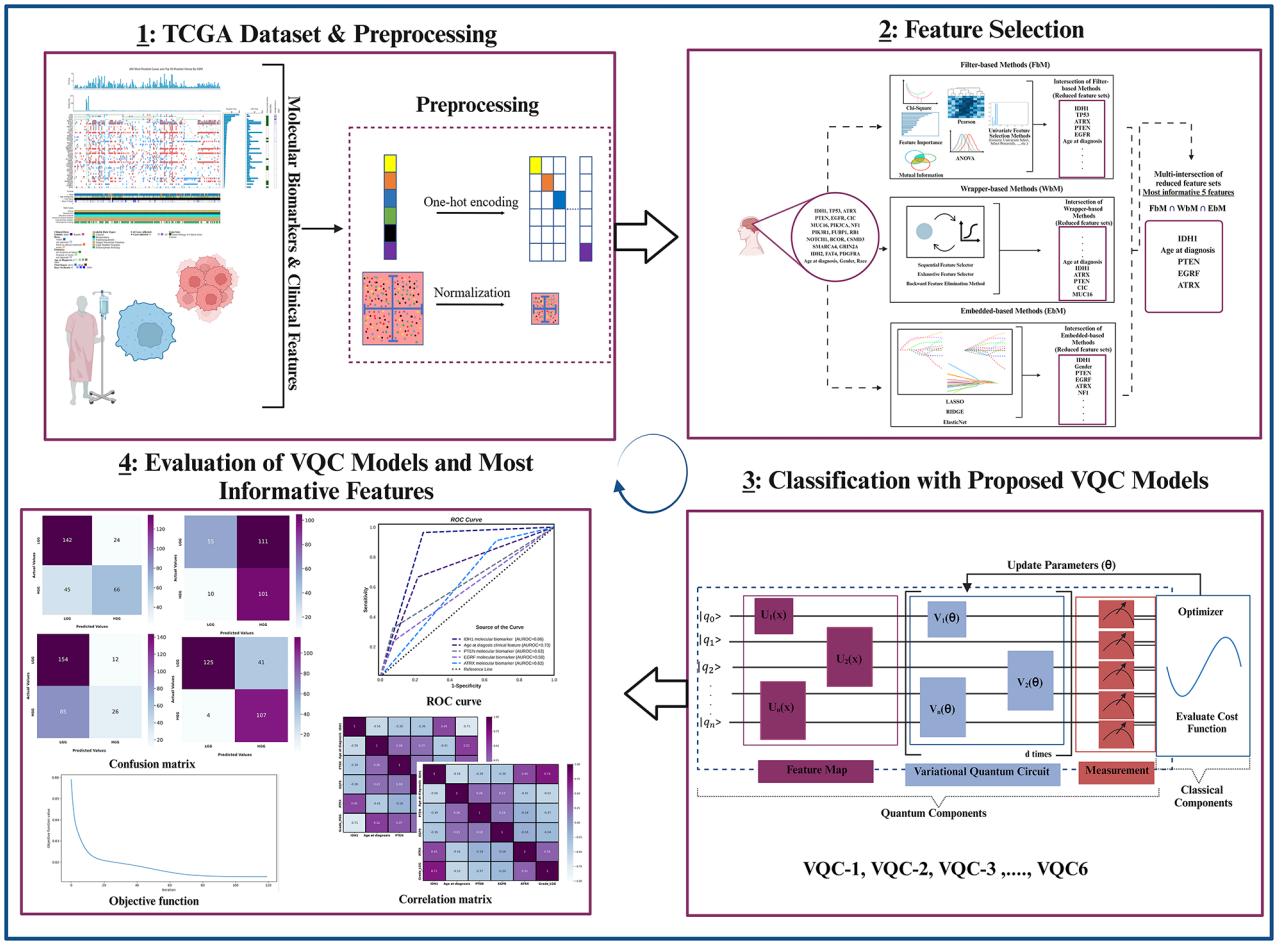



**Fig. 1**. Flowchart of the proposed hybrid classical and quantum computing model to discriminate LGGs from HGGs. (1) TCGA glioma data (molecular biomarkers and clinical features) encoding and normalization. (2) Selection of the most informative features using the ensemble feature selection method. (3) Classification of LGGs and HGGs using six variants of VQC models with different hyperparameters. (4) Evaluation of the classification performance of VQC models and identification of the most informative features.

B), measuring one particle will dictate the values that the properties of the other particle must assume. This indicates that particles A and B are entangled, revealing a correlation between them. In this case, one cannot determine the state of the A or B particles separately[81]. These properties provide quantum computers with a fundamental speed advantage compared to classical computers.

## Dirac (Bra-Ket) notation

Dirac notation was developed for representing quantum states as vectors and operators as matrices and is extensively used in the fields of quantum mechanics and quantum computing[82]. In other words, Dirac notation, which is a standard notation for representing states in quantum mechanics, is used. In Dirac notation, a column vector can be represented as a ket $(|\varphi\rangle)$ and its conjugate transpose as a bra $(\langle\varphi|)$.

In Dirac notation, the inner product of two vectors, $u$ and $v$, can be defined as follows:

$$\langle u|v\rangle \tag{1}$$

Similarly, the outer product (or matrix multiplication) of these two vectors can be defined as,

$$|u\rangle\langle v| \tag{2}$$

The inner product involves taking the conjugate transpose of the first vector, which is denoted with a bra. The outer product, on the other hand, keeps the first vector in column form and takes the conjugate transpose of the second vector.

Additionally, the tensor product can be utilized to represent the state of multiple independent qubits in a register. This operation allows one to express the combined state of these qubits. If two qubits are represented as $a$ and $b$, the tensor of two qubits is,

$$|a\rangle \otimes |b\rangle \\ |a\rangle\,|b\rangle \tag{3}$$

and this way as well,

$$|ab\rangle \tag{4}$$

## Qubit and quantum states

In 1995, the most basic unit of quantum computing was created when Ben Schumacher defined the 'quantum bit' or 'qubit' as a tangible physical resource[83]. Qubits are basic building blocks that encompass all fundamental quantum phenomena. A physical qubit is a two-level quantum mechanical system that includes an electron orbiting a nucleus, a spin state of an electron, and photon polarization[81]. The State Space Postulate asserts that the state of a qubit system can be described by a vector within a 2-dimensional Hilbert space. The Hilbert space is a special type of vector space that can be finite or infinite in dimension and is endowed with an inner product in addition to all the usual rules of vector spaces.

Two possible states for a qubit are $|0\rangle$ and $|1\rangle$. Based on the states of these qubits, it is also feasible to create linear combinations of states (as previously stated, it is called superpositions):

$$\alpha\ |0\rangle\ + \beta\ \ |1\rangle, \tag{5}$$

where $\alpha$ and $\beta$ are complex numbers and are often called the amplitudes of the basis states $|0\rangle$ and $|1\rangle$, respectively. The $|0\rangle$ and $|1\rangle$ bases represent the state of a qubit and are commonly referred to as computational bases in a two-level system. When a measurement is performed on a qubit, the probability of obtaining the $|0\rangle$ state is $|\alpha|^2$, while the probability of obtaining the $|1\rangle$ state is $|\beta|^2$. Naturally, $|\alpha|^2 + |\beta|^2 = 1$, as the probabilities must collectively sum to one. In addition, the states of the qubits are normalized to a length of 1.

In addition to the ket vector representation described above, the states $|0\rangle$ and $|1\rangle$ can also be defined using the following vector notation:

$$|0\rangle = \begin{bmatrix} 1 \\ 0 \end{bmatrix} \\ |1\rangle = \begin{bmatrix} 0 \\ 1 \end{bmatrix}. \tag{6}$$

The most general state of a qubit $\psi$ can be expressed as follows:

$$|\psi\ \rangle = \ cos\left(\frac{\theta}{2}\right)|0\rangle + e^{i\phi}\ sin\left(\frac{\theta}{2}\right)|1\rangle\ , \tag{7}$$

$\theta$ and $\phi$ represent real numbers that define a point on the unit three-dimensional Bloch sphere, as shown in Fig. 2. The Bloch sphere offers a valuable approach for depicting the condition of an individual qubit and frequently functions as an exceptional platform for exploring concepts related to quantum computation and quantum information.

## Quantum gates (quantum data manipulation)

In quantum computation, information is stored in a set of qubits (or quantum registers), and then external fields, such as oscillating magnetic fields, electric fields or laser beams, are applied to produce gate operations on the register. In gate-based quantum computers, the operators or quantum gates used to manipulate the state

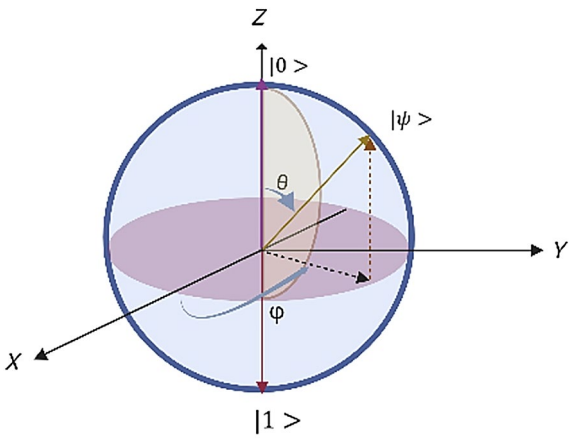



**Fig. 2**. Geometric representation of a qubit's state on the Bloch sphere.

of qubits are unitary and thus reversible. A finite set of quantum gates can generate any arbitrary quantum computation for a given number of qubits.

Quantum gates are commonly categorized as either single-qubit gates or multi-qubit gates, based on the number of qubits to be manipulated[84]. In this study, we used single-qubit gates that operate on individual qubits and multi-qubit gates that operate on two qubits. Matrices of size $2\times2$ can be employed to characterize quantum gates that operate on a single qubit. The appropriate condition for the matrix representing a single-qubit gate is that the matrix $U$ describing the gate satisfies the following condition:

$$U^{\dagger}U = I, \tag{8}$$

where $U^{\dagger}$ is the adjoint of $U$( obtained by transposing and then complex conjugating U) and $I$ is the $2\times2$ identity matrix. In addition, in the context of quantum computing and the Bloch sphere representation, the effect of a 1-qubit quantum gate $U$ on a quantum state $|\psi\rangle$ can be considered a transformation where the Bloch vector of $|\psi\rangle$ is transformed into the Bloch vector of $U|\psi\rangle$.

The single-qubit quantum gates used in our study are as follows:

Pauli gates: Pauli gates, a fundamental concept in quantum computing and quantum information theory, are crucial in the manipulation and processing of quantum data. These gates are especially significant because they form a basis set that spans the vector space of all 1-qubit operators, enabling the representation of various quantum operations as combinations of Pauli gates.

Pauli X gate (Bit-flip operator): The Pauli X gate is also referred to as the Quantum NOT gate. This gate transitions the state vector from one basis state to another. In the Bloch sphere, a π-radian rotation is performed around the x-axis. The matrix representation of this gate can be defined as follows.

$$X = \begin{bmatrix} 0 & 1 \\ 1 & 0 \end{bmatrix} \tag{9}$$

Pauli Y gate: This gate performs a π-radian rotation around the y-axis in the Bloch sphere. The matrix representation of this gate can be defined as follows.

$$Y = \begin{bmatrix} 0 & -i \\ i & 0 \end{bmatrix} \tag{10}$$

Pauli Z gate (Phase-flip operator): The Pauli Z gate performs a π-radian rotation around the z-axis of the Bloch sphere and simultaneously adds a global phase factor while altering the state of the qubit. The matrix representation of this gate can be defined as follows.

$$Z = \begin{bmatrix} 1 & 0 \\ 0 & -1 \end{bmatrix} \tag{11}$$

Hadamard gate: This single-qubit gate is also described as the "square root of NOT", which plays a pivotal role in quantum computing because it allows one to transition a qubit from a well-defined computational basis state into a superposition of two states. The matrix representation of the Hadamard gate is as follows.

$$H = \frac{1}{\sqrt{2}}\begin{bmatrix} 1 & 1 \\ 1 & -1 \end{bmatrix} \tag{12}$$

In addition, the Hadamard gate manipulates the computational basis states as outlined in the following manner.

If the Hadamard gate is applied to the $|0\rangle$ state,

$$\frac{1}{\sqrt{2}}\begin{bmatrix} 1 & 1 \\ 1 & -1 \end{bmatrix}\begin{bmatrix} 1 \\ 0 \end{bmatrix} = \frac{1}{\sqrt{2}}\begin{bmatrix} 1+0 \\ 1+0 \end{bmatrix} = \frac{1}{\sqrt{2}}\begin{bmatrix} 1 \\ 1 \end{bmatrix} = \frac{|0\rangle + |1\rangle}{\sqrt{2}} \tag{13}$$

and to the state $|1\rangle$,

$$\frac{1}{\sqrt{2}}\begin{bmatrix} 1 & 1 \\ 1 & -1 \end{bmatrix}\begin{bmatrix} 0 \\ 1 \end{bmatrix} = \frac{1}{\sqrt{2}}\begin{bmatrix} 0+1 \\ 0-1 \end{bmatrix} = \frac{1}{\sqrt{2}}\begin{bmatrix} 1 \\ -1 \end{bmatrix} = \frac{|0\rangle - |1\rangle}{\sqrt{2}} \tag{14}$$

The state resuting from applying the Hadamard gate to the $|0\rangle$ state, which is represented as $\frac{|0\rangle+|1\rangle}{\sqrt{2}}$, is denoted as $|+\rangle$, and the state resulting from applying the Hadamard gate to the $|1\rangle$ state, which is represented as $\frac{|0\rangle-|1\rangle}{\sqrt{2}}$, is denoted as $|-\rangle$. The set $\{|+\rangle, |-\rangle\}$ is sometimes referred to as the Hadamard basis.

Rotations gates: Many quantum gates, for instance, the standard rotation gates $R_x(\theta)$, $R_y(\theta)$, $R_z(\theta)$ are defined in terms of angles. These gates are used to rotate a quantum state about a specific axis by a certain angle. The rotation gates have matrix representations as follows

$$R_x(\theta) = e^{-iX\frac{\theta}{2}} = \begin{bmatrix} cos\left(\frac{\theta}{2}\right) & -sin\left(\frac{\theta}{2}\right)i \\ -sin\left(\frac{\theta}{2}\right)i & cos\left(\frac{\theta}{2}\right) \end{bmatrix}, R_y(\theta) = e^{-iY\frac{\theta}{2}} = \begin{bmatrix} cos\left(\frac{\theta}{2}\right) & -sin\left(\frac{\theta}{2}\right) \\ sin\left(\frac{\theta}{2}\right) & cos\left(\frac{\theta}{2}\right) \end{bmatrix}, R_z(\theta) = e^{-iZ\frac{\theta}{2}} = \begin{bmatrix} e^{-i\frac{\theta}{2}} & 0 \\ 0 & e^{i\frac{\theta}{2}} \end{bmatrix}. \tag{15}$$

As previously stated, Pauli gates $X$, $Y$, and $Z$ correspond to π-radian rotations about the x-, y-, and z-axes of the Bloch sphere, respectively.

The multi-qubit quantum gates used in our study are as follows:

Controlled-NOT (CNOT) gate: The CNOT (or CX) gate is a two-qubit gate that plays a crucial role in quantum computation. In this binary operator, the first qubit is identified as the control qubit, and the second is identified as the target qubit. The gate flips or X gate to the second qubit (the target qubit) when the first qubit (the control qubit) state is $|1\rangle$, while the second bit is left unchanged when the first qubit state is $|0\rangle$. In addition, CNOT gate is utilized to create entanglement between two qubits in quantum computing. The matrix representation of the CNOT gate is as follows:

$$CNOT\ (CX) = \begin{bmatrix} 1 & 0 & 0 & 0 \\ 0 & 1 & 0 & 0 \\ 0 & 0 & 0 & 1 \\ 0 & 0 & 1 & 0 \end{bmatrix} \tag{16}$$

All the other multi-qubit quantum gates consist of a combination of CNOT and single-qubit quantum gates. Taking this as a reference, we also used CY and CZ multi-qubit gates in this study.

Controlled-Y gate (CY) and Controlled-Z gate (CZ): In the CY and CZ quantum gates, as with the CNOT quantum gate, there are control and target qubits. However, in these operations, when the control qubit is in the state $|1>$, the target qubit is subjected to the Y and Z operators, separately. The matrix representations of these quantum gates are as follows:

$$CY = \begin{bmatrix} 1 & 0 & 0 & 0 \\ 0 & 1 & 0 & 0 \\ 0 & 0 & 0 & -i \\ 0 & 0 & i & 0 \end{bmatrix}, CZ = \begin{bmatrix} 1 & 0 & 0 & 0 \\ 0 & 1 & 0 & 0 \\ 0 & 0 & 1 & 0 \\ 0 & 0 & 0 & -1 \end{bmatrix}. \tag{17}$$

The representations of single-qubit ( $R_x$, $R_y$, $R_z$) and multi-qubit (CX, CY, CZ) quantum gates using different visualization techniques are presented in Fig. 3. The Bloch sphere and Q-sphere provide geometric interpretations of single and two-qubit states, respectively, while quantum circuit structures depict the operation of these gates. Additionally, the matrix representations of quantum gates and the three-dimensional Cityscape plots of qubit state matrices, including their real and imaginary components, are provided to enhance the comprehensive understanding of quantum operations.

### Quantum circuit

In the quantum circuit model, a structure wherein which logical qubits are carried along "wires" exists, and quantum gates act upon these qubits[82]. In other words, this circuit model is expressed as a collection formed by n qubits (say 2) and single-qubit or multi-qubit gates from a universal gate set (e.g., $R_x$, Hadamard, CNOT), where these gates apply unitary operators on these qubits. Each unitary operator or gate is symbolized by a block with lines (or "wires") indicating the input and output. In the quantum computing literature, it is generally assumed that the input state to the circuit is the computational basis state consisting of all $|0\rangle$s. At its most fundamental level, a quantum circuit model is illustrated in Fig. 4. As depicted in the figure, the circuit is read from left to right, and the "wires" are represented as horizontal lines. Here, it can be noted that qubits progress from left to right along the "wires" in time, and different qubit states are obtained based on the applied unitary operators.

## Methods

In this section, a detailed description of the proposed hybrid classical and quantum computing method for distinguishing between LGGs and HGGs is provided. First, a general flowchart of the method is presented (Fig. 1). The approach consists of two main components: classical computing and quantum computing. The classical computing section explains the applied preprocessing and feature selection techniques, while the quantum computing section details the theoretical framework of the proposed variational quantum classifiers (VQCs) used for classification. Although six different VQC models are proposed, they share the same fundamental theoretical structure but differ in their hyperparameters.

### Classical computing

Before advancing to the quantum computation phase, this section focuses on the data preprocessing and feature selection steps. During the preprocessing step, encoding and normalization operations are applied, while in the feature selection step, efforts are made to determine the most informative features.

*Preprocessing*

For effective analysis and modeling, data preprocessing plays a pivotal role in enhancing the quality and reliability of our dataset. In this way, prior to training and executing any algorithms and methods, it is necessary to verify the data's representation. In this study, following the determination of categorical values, such as "MUTATED" and "NOT_MUTATED" gene expressions, in the TCGA dataset, these values were converted to numerical values using the *one-hot encoding* method.

After all the numerical values were obtained, normalization process was applied to the features. Normalization in quantum ML is essential for maintaining quantum state consistency, reducing the impact of quantum noise, facilitating efficient quantum computations, and enabling meaningful comparisons of quantum states[85]. Briefly, ensuring the reliability and effectiveness of quantum algorithms is a fundamental step. In the present study, the min-max normalization technique was employed to rescale the data features to a specific range while preserving

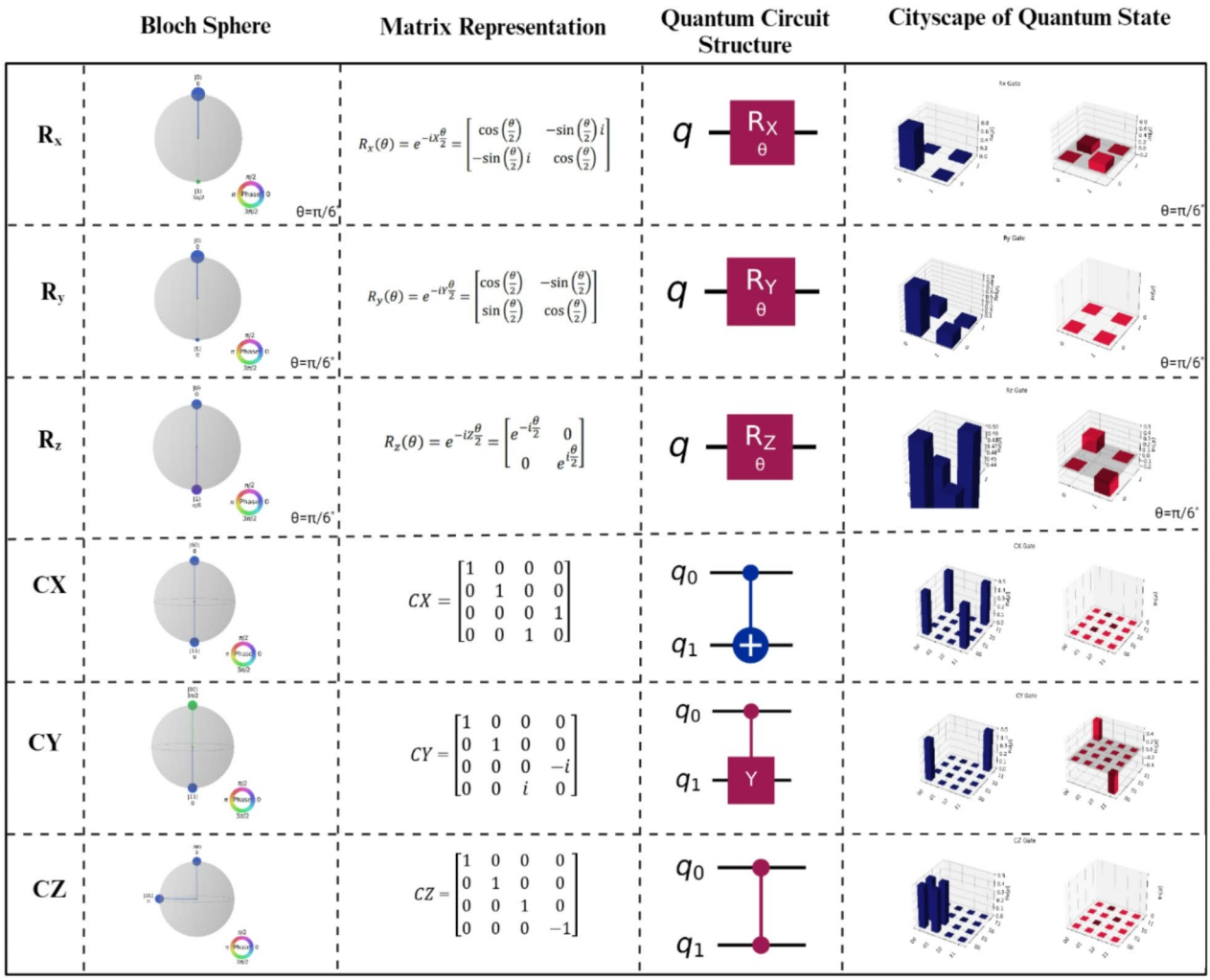



**Fig. 3**. This figure illustrates various representations of single-qubit ($R_x$, $R_y$, $R_z$) and two-qubit (CX, CY, and CZ) quantum gates. In the top left corner, the Bloch sphere geometrically depicts the possible states of single qubits and two qubits (Q-sphere). The second and third sections show the matrix representations of qubits and circuit structures, respectively, that represent interactions between qubits. Finally, in the top right corner, Cityscape presents three-dimensional plots of qubit state matrices, with one graph for the real parts and another for the imaginary parts. Furthermore, the representations for single qubits were provided with specific examples, such as $\theta = \pi/6$.

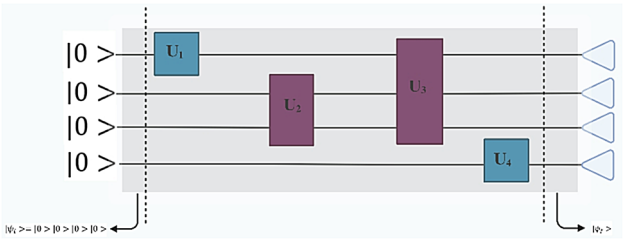



**Fig. 4**. An illustration of a general quantum circuit. $U_1$ and $U_4$ denote single-qubit unitary quantum gates, and $U_2$ and $U_3$ represent multi-qubit unitary quantum gates. The above figure also depicts the evolution of a quantum state $|\psi_i\rangle$ to $|\psi_f\rangle$ according to a unitary operator U.

their original distributions. Min-max normalization assigns data features to a certain minimum and maximum range. This method is usually applied using the following formula:

$$x_{normalize} = \frac{(x - \min(x))}{(\max(x) - \min(x))} \tag{18}$$

In here, $x_{normalize}$ represents the normalized value; $x$ represents the original value; $\min(x)$ , is the minimum value; and $\max(x)$, is the maximum value of the data feature.

*Feature selection*

Identifying the most informative molecular biomarkers and clinical features, as well as selecting small feature sets with high classification accuracy, is crucial both for minimizing the cost of classification and for gaining biological insight[86]. Therefore, the most informative features for distinguishing between LGGs and HGGs were filtered using feature selection methods. Feature selection methods aim to reduce the number of features and identify input variables most robustly correlated with output variables. This decrease in the number of selected features also greatly impacts the performance of the model[87–89]. In this context, a total of 19 methods belonging to the categories of *filter-based*, *embedded-based*, and *wrapper-based*[89–92] feature selection techniques were employed in our study.

Filter-based methods: Filter-based methods ( $\mathrm{FbM}$) utilize an evaluation function based on the characteristics of the data, independent of modeling algorithms and without considering interactions with the classifier. Each feature is assessed individually using statistical criteria. Additionally, filter methods do not select the optimal feature subset; instead, they rank the entire set of features, and the selection process is left to the user. Since this approach employs independent statistical measures without incorporating a learning algorithm (e.g., a classifier), it is computationally more efficient and faster. However, this independence also means that dependencies and interactions among features are overlooked, which may affect classification performance.

The filter-based feature selection methods used in this study are as follows:

Information Gain, Generic Univariate Select, Select Percentile, Select False Discovery Rate (SelectFdr), Select False Positive Rate (SelectFpr), Select Family Wise Error (SelectFwe), F-Score, Recursive Feature Elimination, Chi-Squared Best, Mutual Information Filter-Based Method, Feature Importance, ANOVA, and Correlation-Based Feature Selection (Pearson).

Wrapper-based methods: Wrapper-based methods ( $\mathrm{WbM}$) evaluate feature subsets using a predefined learning model. In this process, a greedy search strategy is typically employed to select the feature set, and various feature combinations are assessed. The training process follows an iterative structure, where the feature subset used in the previous step is reviewed based on model performance. Depending on performance, certain features are either added to or removed from the subset. Consequently, the training process is completed once the algorithm reaches a feature subset with the target number of features specified by the user. Unlike filter-based methods, wrapper methods take feature dependencies into account and analyze the interaction between feature selection and model performance. However, due to their iterative nature, the repeated invocation of the classifier model can make wrapper methods prone to overfitting. Additionally, especially in high-dimensional datasets, the application of these methods can significantly increase computational costs.

The wrapper-based feature selection methods used in this study are as follows:

Sequential Feature Selector, Exhaustive Feature Selector, Backward Feature Elimination Method.

Embedded-based methods: Embedded-based methods ( $\mathrm{EbM}$) operate similarly to wrapper methods in identifying the most important feature subsets; however, the key difference is that feature selection occurs during the model training process. In other words, the feature selection step is integrated into the classifier's training phase. As a result, both a selected feature subset and a trained classifier are obtained at the end of the process. These methods offer advantages in terms of faster training and lower computational cost while being less prone to overfitting compared to wrapper methods. However, the generalization capability of the selected features may be limited depending on the type of model used, as the feature selection process is influenced by the classifier's hypothesis.

The embedded-based feature selection methods used in this study are as follows:

LASSO (Least Absolute Shrinkage and Selection Operator), RIDGE (Ridge Regression), ElasticNet.

However, each feature selection method mentioned above determines and ranks features differently, and each selected feature reflects a different aspect of the dataset[93]. Moreover, some selected features may yield better solutions to specific problems. As a solution to this problem, the strategy we employed in our study aims to combine various feature selection methods (or ensemble feature selection) to capture different profiles of features and obtain more useful information for classification.

In *Ensemble feature selection*, different reduced feature sets are generated in conjunction with filter, wrapper, and embedded feature selection techniques. These reduced feature sets are subsequently combined via a multiple intersection method.

If the original feature set ( $S$) is defined as,

$$S = \{f_1,\ f_2, f_3 \ldots .,f_{23}\} \tag{19}$$

The first step involves applying filter, wrapper, and embedded feature selection methods simultaneously to the original feature set. These methods aim to select a subset of features deemed most relevant or informative for the classification task. Each method ranks the features based on its own selection criteria and selects the top 10 most relevant features as follows;

$$\begin{aligned} FbM_{10} &= \{f_{a1},\ f_{a2},\ \ldots.,f_{a10}\ \} \\ WbM_{10} &= \{f_{b1},\ f_{b2},\ \ldots.,f_{b10}\ \} \\ EbM_{10} &= \{f_{c1},\ f_{c2},\ \ldots.,f_{c10}\ \} \end{aligned} \tag{20}$$

The selection of 10 features was guided by both the feature selection results and K-fold cross-validation (K = 10) performance observed across different classifiers, including support vector classifier (SVC), random forest classifier (RFC), and logistic regression (LR) (as presented in Supplementary Table 1). The performance of these ML algorithms was evaluated for K values of 5, 10, 15, and 20, with K = 10 demonstrating the lowest variance and highest accuracy. Since this setting provided an optimal balance between accuracy and model generalizability, the number of selected features was aligned with the chosen K-fold value.

Next, within each feature selection method, an intersection process is applied to determine the most consistently selected features. This is mathematically represented by the following equations, where $n_F$, $n_W$ and $n_E$ represent the number of features selected by each method (which is 10 in this case):

$$\begin{aligned} FbM_{\cap} &= \bigcap_{i=1}^{n_F} FbM_i \\ WbM_{\cap} &= \bigcap_{i=1}^{n_W} WbM_i \\ EbM_{\cap} &= \bigcap_{i=1}^{n_E} EbM_i \end{aligned} \tag{21}$$

In the final step, the reduced feature sets obtained from the three selection categories are further merged using a multiple intersection method to determine the most informative features. The final selected most informative 5 features are IDH1, age at diagnosis, PTEN, EGFR, and ATRX.

$$\begin{aligned} S_{final} &= FbM_{\cap} \cap WbM_{\cap} \cap\ EbM_{\cap}, \text{or} \\ S_{final} &= \{\text{IDH1},\ \text{Age at diagnosis},\ \text{PTEN},\ \text{EGFR},\ \text{and ATRX}\} \end{aligned} \tag{22}$$

In Fig. 5, a detailed representation of the ensemble feature selection method used in our study is available.

## Quantum computing

In this section, within the VQC circuit, the data samples are initially encoded from the classical vector space into the quantum Hilbert space through feature maps. In this study, two qubit-efficient methods, angle encoding, and Pauli feature maps, are introduced and described in detail in the following sections. Following the feature maps, detailed information has been provided about the classification process involving the variational circuit or parameterized quantum circuit, and the circuit structures used in our study have been discussed. Finally, the section concludes with the measurement and optimization processes.

*State preparation or feature mapping*

Quantum feature mapping is a pivotal concept in the realm of quantum ML, offering a transformative approach to encoding and manipulating classical data within quantum computational frameworks[94–96]. Quantum computers can only interact with data expressed as quantum states; therefore, classical data must be transformed into quantum states for processing by quantum algorithms. If we define $S(x)$ as a data embedding circuit that depends on the classical data point $x(\ x \in\ X)$ from some domain $X$ to prepare a quantum state[97],

$$S(x)\,|0\rangle^{\otimes n} \ =\ |\varphi\ (x)\rangle = |\varphi\ (x)\rangle\,\langle\varphi\ (x)|\,. \tag{23}$$

This circuit acts on an initial state $\varphi\ (x)$, which is nominally all zero states $|\varphi\ (x)\rangle = |0\rangle^{\otimes n}$. The number of qubits, denoted as 'n', is determined by the total count of features present within our dataset. In our study, the feature mapping methods employed to nonlinearly embed classical data from the classical vector space into a potentially much higher-dimensional feature space, namely, the quantum Hilbert space, are as follows:

Angle encoding (or rotation encoding): Angle encoding is one of the fundamental feature encoding methods. In this technique, N qubits are utilized with a constant-depth quantum circuit, making it suitable for NISQ computers. Here, the number of qubits, denoted as N, depends on the amount of data, requiring one qubit per component of the input vector[98] $(x_i)$. Moreover, state preparation exhibits notable efficiency in temporal terms, as it necessitates only single-qubit rotation gates[99].

In particular, all the data were normalized to the range $[0,\ 2\pi\,]$. Each classical data value $x_i$ was then represented by a single qubit as follows:

$$\begin{aligned} x_i &= \cos\left(\frac{x_i}{2}\right)|0\rangle + \sin\left(\frac{x_i}{2}\right)|1\rangle\,, \\ x_i &= \cos(\theta)\,|0\rangle + \sin(\theta)\,|1\rangle \end{aligned} \tag{24}$$

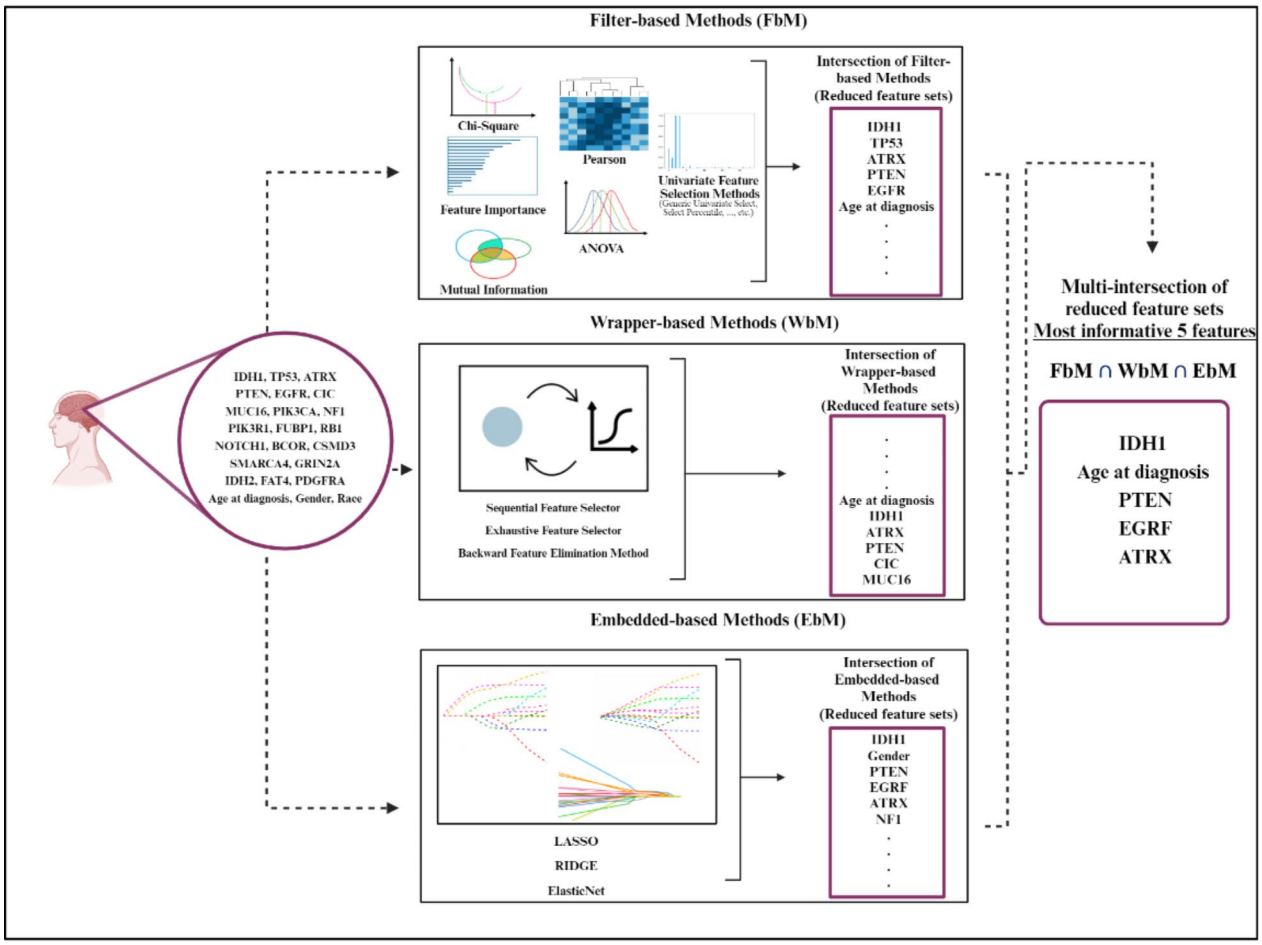



**Fig. 5**. A schematic representation of the ensemble feature selection process: The original feature set, consisting of 23 molecular and clinical features, is simultaneously processed using filter, wrapper, and embedded feature selection methods. Each method ranks the features based on its own selection criteria and selects the top 10 most relevant features. Within each method, a refined feature subset is obtained by applying an intersection operation. In the final step, the most informative five features are determined through a multi-intersection approach, ensuring robust and consistent feature selection.

Here, the rotation angle is determined by the data. In this study, we employed rotational gates; $R_x(x_i)$, $R_y(x_i)$, $R_z(x_i)$. For example, if we make use of the matrix representations of the $R_y$ rotational gate, as described in "Quantum gates (quantum data manipulation)", along with the vector representations of the $|0\rangle$ and $|1\rangle$ kets, we can apply $R_y$ rotational gates to these computational basis states, as demonstrated in Eqs. (25) and (26).

$$R_y(x_i)|0\rangle = e^{-iY\frac{x_i}{2}}|0\rangle = \begin{bmatrix} cos\left(\frac{x_i}{2}\right) & -sin\left(\frac{x_i}{2}\right) \\ sin\left(\frac{x_i}{2}\right) & cos\left(\frac{x_i}{2}\right) \end{bmatrix} \begin{bmatrix} 1 \\ 0 \end{bmatrix} = cos\left(\frac{x_i}{2}\right)|0\rangle + sin\left(\frac{x_i}{2}\right)|1\rangle \quad (25)$$

$$R_y(x_i)|1\rangle = e^{-iY\frac{x_i}{2}}|1\rangle = \begin{bmatrix} cos\left(\frac{x_i}{2}\right) & -sin\left(\frac{x_i}{2}\right) \\ sin\left(\frac{x_i}{2}\right) & cos\left(\frac{x_i}{2}\right) \end{bmatrix} \begin{bmatrix} 0 \\ 1 \end{bmatrix} = cos\left(\frac{x_i}{2}\right)|1\rangle - sin\left(\frac{x_i}{2}\right)|0\rangle \quad (26)$$

In summary, the use of angle encoding methods in this study is due to their properties, which provide low resource requirements and high computational efficiency, scaling linearly with the data size (one qubit per input component, $x_i$). Additionally, these methods avoid qubit entanglement and perform state preparation solely with single-qubit rotational gates, offering advantages in terms of circuit depth and execution time.

Pauli feature mapping: In this study, we used ZZFeatureMap, which is a second-order expansion of the Pauli feature map ($U_\phi(\vec{x_i})$).

$$U_{\phi\,(\vec{x_i})} = exp\left(i\sum\nolimits_{S\subseteq\,[n]} \phi_{\,S}\,(\vec{x})\prod\nolimits_{\,i\in\,S} P_i\right) \tag{27}$$

where $P_i$ denote the Pauli matrices and $P_i \in \{I, X, Y, Z\}$ and $S$ define the connectivity between different qubits[57,100]. If we customize the Pauli gates as $P_0 = X,\ P_1 = Y, and\ P_2 = ZZ$, ZZFeatureMap is obtained as follows:

$$U_{\phi\,(\vec{x_i})} = \left(exp\left(i\sum\nolimits_{jk} \phi_{\,(\{j,k\}}\,(\vec{x})\,Z_j \otimes\ Z_k\right) exp\left(i\sum\nolimits_{j} \phi_{\,\{j\}}\,(\vec{x})\,Y_j\right) exp\left(i\sum\nolimits_{j} \phi_{\,\{j\}}\,(\vec{x})\,X_j\right) H^{\otimes\,n}\right)^{d} \tag{28}$$

The ZZ feature map efficiently utilizes quantum resources by representing $n$ features with $n$ qubits. Moreover, due to its entanglement structure, this map provides a quantum advantage as it cannot be classically simulated at large scales. This makes ZZ feature map particularly suitable for efficient quantum computing applications in the context of this study.

## Variational circuit (parametrized quantum circuit)

A variational circuit, also known as a parametrized quantum circuit (PQC), is a hybrid quantum-classical circuit that incorporates a combination of parametrized (or non-parametrized) and fixed one- and two-qubit unitary quantum gates, defining the circuit's architecture[58,71,75,101–103]. The first strategy in circuit design aims to accommodate the constraints of NISQ hardware, which typically involves a limited number of qubits, operates on a sparsely connected qubit-to-qubit connectivity graph, and has relatively simple gates. Thus, PQC provides a tangible approach to implementing algorithms and demonstrating quantum supremacy in the NISQ era[101–104]. PQC is used in various quantum ML applications, including classification, as explored in this study. Furthermore, with trainable parameters or weights in circuits, PQC conceptually resembles a traditional neural network. However, despite their similar working principles, they have two fundamental differences, as outlined below[101]:

- The first key difference is that quantum circuit operations are unitary and therefore linear.
- The second key difference lies in the impossibility of accessing the quantum state at intermediate points during computation.

Similar classical models, PQC models are trained to execute data-driven tasks. PQC, also denoted as $W\,(\theta\,)$, is composed of $U_{rot}$, which is a $n$ single qubit unitary $R\,(\theta_{\,i})$ and $U_{ent}$ which is defined as blocks of two qubit gates that can introduce entanglement[100,102,105]. $W\,(\theta\,)$ is defined as follows:

$$W\,(\theta\,) = U^{l}_{rot}\,(\theta_{\,l})\ U_{ent} \ldots\ U^{2}_{rot}\,(\theta_{\,l})\ U_{ent} U^{1}_{rot}\,(\theta_{\,l})\ U_{ent} \tag{29}$$

In this context, "$l$" represents the depth of the variational circuit, and parameter vector $\theta$ represents the learnable variable. The structure of the PQC is presented in Fig. 6. The parameters $\theta_{\,l}$ can be optimized by minimizing a cost function or objective function ($L\,(\theta\,)$), which adjusts the gates and consequently the circuit to address a specific problem. In this study, the single-qubit rotations are associated with $R_x$, $R_y$, and $R_z$ rotations, while the $U_{ent}$ block comprises CX and CY, CZ gates.

## Measurement

The measurement phase is alternatively referred to as the decoding phase, playing a crucial role in converting quantum data into classical form. This phase is important for predicting class labels and obtaining class probabilities. In this stage, for the two-label classification $y \in \{+1, -1\}$ problem, a binary measurement operator $\{M_y\}$ is applied to state $W\,(\theta\,)\,U_{\phi\,(\vec{x_i})}|0\rangle^n$. In our study, this measurement is implemented on a computational basis or on a *Pauli Z* basis[100,106]. The binary measurement is derived from the parity function, $f = Z_1 Z_2$. The results, which are bit strings, $z \in \{0,\ 1\}^n$, are assigned to a label based on a predetermined Boolean function. $f = \{0,\ 1\}^n \rightarrow\ \{+1,\ -1\}$. In brief, the process works as follows:

- Measuring the circuit outcome,
- Computing the parity of the bit string,
  - If the measurement consisted of an even number of '1's, it will be mapped to the HGGs class,
  - If the measurement outcome consisted of an odd number of '1's, it will be mapped to the LGGs class.

To stabilize the stochastic effects of the measurements, the quantum circuit will be measured a number of times (or shot) to estimate the probability of its outcomes.

## Optimization

In quantum ML models, as in classical models, it is necessary to update the parameters to minimize the difference between the predicted and actual values. More specifically, once the measurement results are obtained, the parameters ($\theta$) of the variational circuit are adjusted using an optimization routine. The parameter updates continue within a classical loop until the cost function reaches its minimum value. In our study, we used two optimizers: Analytic Quantum Gradient Descent (AQCD)[107] and Spall's simultaneous perturbation stochastic approximation (SPSA)[108].

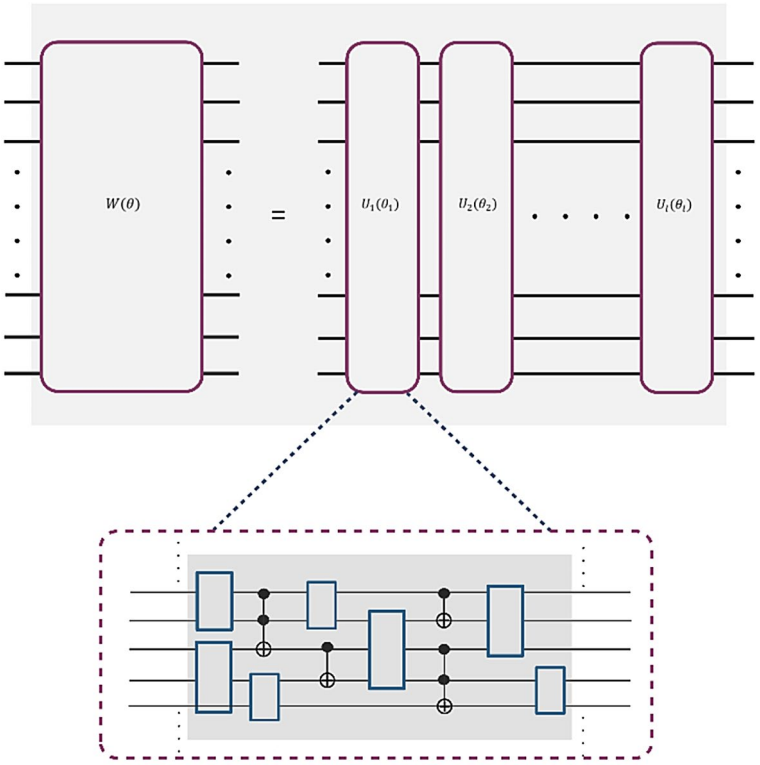



**Fig. 6**. Schematic representation of a variational or parameterized quantum circuit. The unitary $W(\theta)$ expressed with a parameter set $\theta$ consists of a sequence of $L$ unitaries $U_l(\theta_l)$ acting sequentially on an input state. As depicted, each unitary $U_l(\theta_l)$ can be decomposed into a series of parameterized and unparameterized gates.

## Experimental work

This section provides information about the experimental processes, the TCGA dataset with molecular markers and clinical features, and the evaluation metrics.

### Experimental process

Due to the availability of cloud-based backends in the IBMQ, the proposed work was initially carried out on the IBM Quantum Experience platform using the Qiskit 0.36.1 and Python 3.7 frameworks; however, it was later re-executed on the Perlmutter supercomputer using Qiskit 1.2.4 and Python 3.11.7 frameworks. The results obtained are based on computations performed on the Perlmutter supercomputer at NERSC. The machine used for carrying out the processes was equipped with a 12th Gen Intel(R) Core(TM) i5 processor and 8.0 GB of RAM.

### Dataset

In our study, we used the most widely employed and publicly available genome atlas database, The Cancer Genome Atlas (TCGA), for distinguishing between LGGs and HGGs. 862 patients' data were retrieved from the TCGA Research Network (https://www.cancer.gov/tcga). TCGA catalogs and publicly shares significant genomic alterations that cause cancer in large cohorts of human tumors, including brain tumors. In particular, the TCGA-GBM and TCGA-LGG datasets, which contain comprehensive genetic and clinical information on glioma patients, have formed the basis of many studies, including our study, due to their reliability and accessibility. The original dataset from TCGA includes a total of 23 features, comprising 3 clinical features, the top 20 most frequently mutated molecular features, and class labels for glioma grading, as illustrated in Figs. 7 and 8. The clinical information for the patients included *age at diagnosis*, *gender*, and *race*. In addition, the molecular markers for the patients included Isocitrate Dehydrogenase 1 (IDH1), Tumor Protein p53 (TP53), ATRX chromatin remodeler (ATRX), Phosphatase and Tensin Homolog (PTEN), Epidermal Growth Factor Receptor (EGFR), Capicua Transcriptional Repressor (CIC), mucin 16, cell surface associated (MUC16), Phosphatidylinositol-4,5-Bisphosphate 3-Kinase Catalytic Subunit Alpha (PIK3CA), Neurofibromin 1 (NF1), Phosphoinositide-3-Kinase Regulatory Subunit 1 (PIK3R1), Far Upstream Element Binding Protein 1 (FUBP1), RB Transcriptional Corepressor 1 (RB1), Notch Receptor 1 (NOTCH1), BCL6 Corepressor (BCOR), CUB and Sushi Multiple Domains 3 (CSMD3), SWI/SNF Related, Matrix Associated, Actin Dependent Regulator of Chromatin, Subfamily A, Member 4 (SMARCA4), Glutamate Ionotropic Receptor NMDA Type Subunit 2 A (GRIN2A), Isocitrate Dehydrogenase 2 (IDH2), FAT Atypical Cadherin 4 (FAT4), Platelet Derived Growth Factor Receptor Alpha (PDGFRA). Out of 862 patients, 23 were excluded from the dataset due to missing information

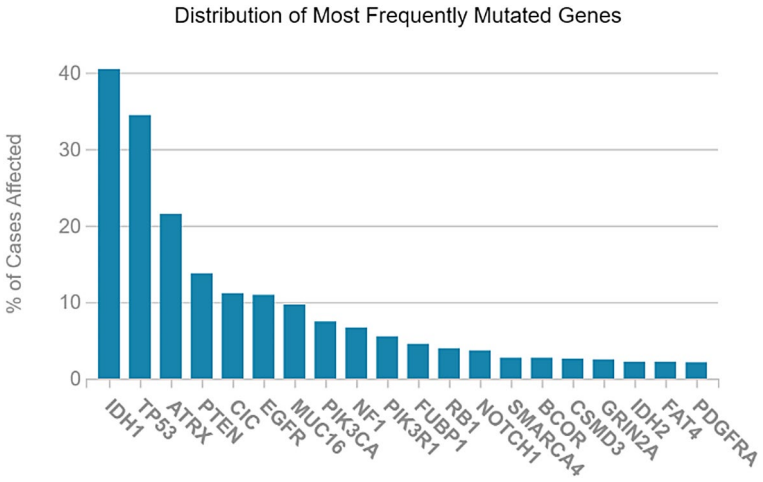



**Fig. 7**. Distribution of the 20 most frequently mutated genes in TCGA glioma dataset, highlighting IDH1, TP53, ATRX, and other key molecular markers.

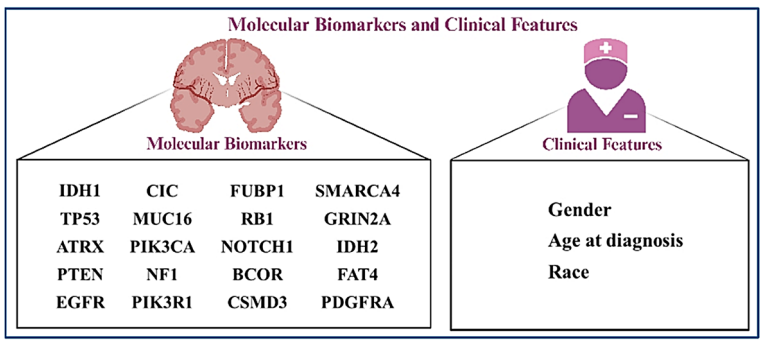



**Fig. 8**. Molecular biomarkers and clinical features from the TCGA glioma dataset used in this study. The figure presents key genetic mutations (e.g., IDH1, TP53, ATRX, PTEN, EGFR) and clinical parameters (e.g., age at diagnosis) that are crucial for glioma classification.

on *age at diagnosis* and *gender*. The remaining dataset included a total of 839 patients, 487 of whom were LGG patients, and the remaining 352 contained information related to HGG patients. The molecular features were recorded as either "MUTATED" or "NOT_MUTATED (wild type)" based on the TCGA case number. These data were subsequently transformed into numerical values during the preprocessing step ("Preprocessing").

## Evaluation metrics

The performances of the proposed VQC models with different hyperparameters were assessed using standard performance metrics, including the receiver operating characteristic curve (AUROC), accuracy, precision, recall and F1-score. The AUROC helps in assessing the trade-off between the true positive rate and false positive rate. The confusion matrix provides more detailed information on how well the prediction model performs, including true positives (TP), true negatives (TN), false positives (FP), and false negatives (FN). These terms can be defined as follows:

1. TP represents the number of HGG patients correctly classified by the proposed VQC models and are labeled HGG.
2. TN, represents the number of LGG patients correctly classified by the proposed VQC models and are labeled LGG.
3. FP represents the number of LGG patients incorrectly classified by the proposed VQC models and are labeled HGG.
4. FN represents the number of HGG patients incorrectly classified by the proposed VQC models and are labeled LGG.

$$Accuracy = \frac{TP + TN}{TP + TN + FP + FN} \tag{30}$$

$$\text{Precision} = \frac{TP}{(TP + FP)} \tag{31}$$

$$Recall = \frac{TP}{(TP + FN)} \tag{32}$$

$$F1 - score = \frac{2 * TP}{(2 * TP + FP + FN)} \tag{33}$$

## Experimental results

In this section, the experimental results are presented in numerical terms. First, during the feature selection phase, the most informative molecular biomarkers and clinical features in the TCGA dataset were identified using an ensemble-based strategy. Subsequently, using these selected features, six VQC models with different hyperparameters were trained to distinguish between LGGs and HGGs, and their performance was evaluated using accuracy, precision, recall, and F1-score metrics. In the next step, the most informative features' impact on the classification of LGGs and HGGs was analyzed using the VQC model that achieved the highest classification performance, and the correlation between these features and glioma tumor grade was examined. Finally, to provide a more comprehensive assessment, a comparative analysis of the classification performance of classical ML models is presented at the end of this section.

### Feature selection

The original TCGA dataset consists of 23 features encompassing 3 clinical attributes, namely, *age at diagnosis*, *gender*, *and race*, along with the 20 most common molecular features (or genomic) denoted as mutated/non_mutated based on TCGA case numbers. These molecular features include *IDH1*, *TP53*, *ATRX*, *PTEN*, *EGFR*, *CIC*, *MUC16*, *PIK3CA*, *NF1*, *PIK3R1*, *FUBP1*, *RB1*, *NOTCH1*, *BCOR*, *CSMD3*, *SMARCA4*, *GRIN2A*, *IDH2*, *FAT4*, *and PDGFRA*. For both cost and biological insight, identifying the most informative genes and clinical data is crucial for distinguishing between HGGs and LGGs. With this aim, a total of 19 feature selection methods were used in this paper, as described in "Methods". The ensemble-based model, incorporating all 23 features from 19 different feature selection methods based on molecular and clinical characteristics, was designed to generate the optimal model for fitting the input data and identifying the most discriminative features between LGGs and HGGs. The 5 most significant features revealed by the ensemble-based model were *IDH1*, *age at diagnosis*, *PTEN*, *ATRX*, *and EGRF*. (Fig. 5).

### Classification performance of VQC models

In this section, of the paper, an attempt was made to obtain an optimal circuit design with minimal quantum gates and circuit depth while ensuring compatibility with NISQ computers by changing hyperparameters such as feature maps, PQC structures, and optimization methods within the VQC framework. The circuit configurations and hyperparameters of the six VQC models are detailed in Supplementary Figs. 1–3. The VQC models are named VQC-1 through VQC-6 based on these hyperparameters. Among these models, the VQC-1 model, with a feature map incorporating $R_x$rotational and CX gates, a parameterized quantum circuit including $R_y$, $R_z$, CY gates, and utilizing the AQCD optimization method for parameter updates, provided the highest classification performance, with an accuracy score of 0.74. In this model, for the LGGs class, the precision, recall, and F1 score were 0.74, 0.87, and 0.80, respectively, whereas for the HGGs class, the precision, recall, and F1 score were 0.74, 0.71, and 0.74, respectively. The VQC-2 model demonstrated secondary predictive performance with an accuracy of 0.72. In the VQC-2 model circuit, $R_y$rotational and CY gates are employed within the feature map, and in the parameterized quantum circuit, $R_y$, $R_z$rotational, and CY gates are utilized. In this model, parameter updates are performed using the AQGD optimization method. In the context of the VQC-2 model, the precision, recall, and F1 score values for the LGGs class were 0.68, 0.99, and 0.81, respectively. In contrast, for the HGGs class, the corresponding values for precision, recall, and F1 score are 0.95, 0.52, and 0.47, respectively. Among these classifiers, the VQC-6 model exhibited the lowest performance, with an accuracy of 0.58. In this model circuit, ZZFeatureMap, which is a Pauli feature mapping method, is employed within the feature map, and in the parameterized quantum circuit, $R_y$ rotational and CY gates are utilized. The parameters are updated using the SPSA optimizer. Within the framework of the VQC-6 model, the LGGs class exhibited precision, recall, and F1 score values of 0.60, 0.91, and 0.72, respectively. Conversely, the HGGs class demonstrated precision, recall, and F1 score values of 0.41, 0.40, and 0.46, respectively. Table 1 lists the performance values of all the classifier models, from VQC-1 to VQC-6. Figures 9 and 10, respectively, display the confusion matrix and loss graph of the VQC-1 model, which yields the highest classification accuracy in distinguishing between LGGs and HGGs when using the most informative 5 features.

To further validate the robustness and generalization capability of the VQC-1 model, a separate 5-fold cross-validation analysis was conducted, resulting in an average accuracy of 0.83. The corresponding average precision, recall, and F1 score values are 0.79, 0.78, and 0.78, respectively. The table presenting the average precision, recall, and F1 score values for each class is provided in Supplementary Tables 2, and the confusion matrix is shown in Supplementary Fig. 4.

### Classification performance of most informative features and correlation analysis between most informative features and glioma tumor grade

In this section, the ability of each of the five most informative features to distinguish LGGs from HGGs was investigated using the best VQC model, VQC-1. In other words, classification was performed by using only one feature at a time, and the performance of each feature was evaluated and compared. As defined in the previous

| | Accuracy | Precision | Recall | F1-score |
|---|---|---|---|---|
| For LGG | | | | |
| VQC-1 | 0.74 | 0.74 | 0.87 | 0.80 |
| VQC-2 | 0.72 | 0.68 | 0.99 | 0.81 |
| VQC-3 | 0.70 | 0.88 | 0.58 | 0.70 |
| VQC-4 | 0.68 | 0.65 | 0.99 | 0.79 |
| VQC-5 | 0.65 | 0.78 | 0.57 | 0.66 |
| VQC-6 | 0.58 | 0.60 | 0.91 | 0.72 |
| For HGG | | | | |
| VQC-1 | 0.74 | 0.74 | 0.71 | 0.74 |
| VQC-2 | 0.72 | 0.95 | 0.52 | 0.47 |
| VQC-3 | 0.70 | 0.60 | 0.88 | 0.71 |
| VQC-4 | 0.68 | 0.92 | 0.42 | 0.35 |
| VQC-5 | 0.65 | 0.54 | 0.77 | 0.63 |
| VQC-6 | 0.58 | 0.41 | 0.40 | 0.46 |

**Table 1**. Performance evaluation results for classifying LGGs and HGGs using VQC models (VQC-1 to VQC-6). The reported performance metrics include accuracy, precision, recall, and F1-score for each model.

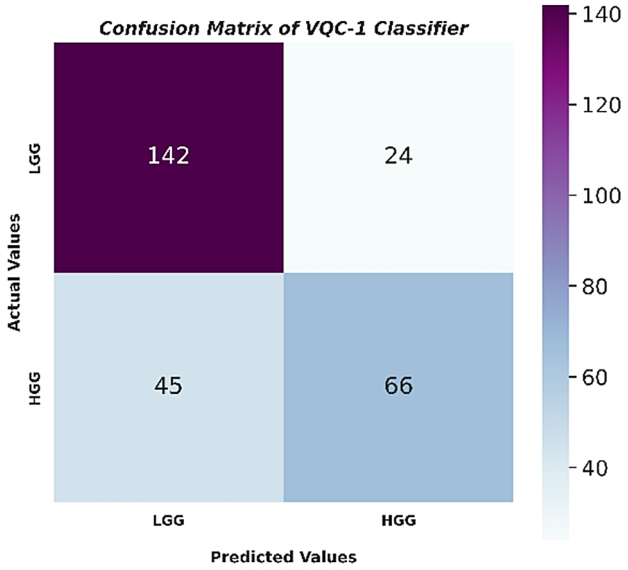



**Fig. 9**. The confusion matrix of the VQC-1 model which yielded the highest classification accuracy in distinguishing between LGGs and HGGs.

section, in the VQC-1 model circuit, $\boldsymbol{R_x}$ rotational and CX gates are employed within the feature map, while in the parameterized quantum circuit, $\boldsymbol{R_y}$, $\boldsymbol{R_z}$ rotational, and CY gates are utilized, and the AQGD optimization method was used for updating the parameters. The *IDH1* molecular marker had the highest accuracy (0.84), followed by the *age at diagnosis* clinical feature (0.74). The accuracy values for the other three most informative molecular features, namely, *PTEN*, *EGRF*, and *ATRX*, in distinguishing between LGGs and HGGs were 0.69, 0.65, and 0.56, respectively. With respect to the proposed model, which included the most informative molecular and clinical features, for LGGs, the precision ranged from 0.64 to 0.97, the recall varied from 0.33 to 0.93, and the F1-score ranged from 0.48 to 0.85. On the other hand, for HGGs, the precision changes from 0.48 to 0.75, the recall ranges from 0.23 to 0.96, and the F1-score varies from 0.35 to 0.65. The results of the performance metrics for the top 5 features are provided in more detail in Table 2. The receiver operating characteristic (ROC) curve and confusion matrix of the 5 most informative molecular biomarkers and clinical features identified using the VQC-1 model for differentiating LGGs from HGGs are illustrated in Figs. 11 and 12, respectively.

The *IDH1* molecular feature showed the highest negative correlation with glioma tumor grade ($r = -0.71$, Pearson's correlation test). Furthermore, Pearson correlation analysis revealed a notable inverse correlation between the *ATRX* molecular feature and glioma tumor grade ($r = -0.31$). The remaining 3 most informative features exhibited a positive correlation with glioma tumor grade. The *age at diagnosis* had the strongest positive correlation with glioma grade ($r = 0.52$), followed by the *PTEN* molecular feature ($r = 0.37$). The *EGFR* molecular

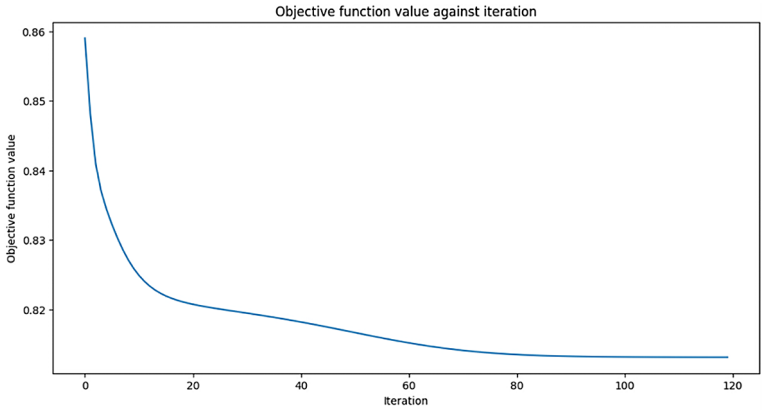



**Fig. 10**. Loss curve of the VQC-1 model during training. The graph shows the model's convergence behavior over epochs, demonstrating stabilization after approximately 60 epochs.

| | Accuracy | Precision | Recall | F1-score |
|---|---|---|---|---|
| For LGG | | | | |
| IDH1 | 0.84 | 0.97 | 0.75 | 0.85 |
| Age at diagnosis | 0.74 | 0.78 | 0.78 | 0.79 |
| PTEN | 0.69 | 0.67 | 0.93 | 0.78 |
| EGRF | 0.65 | 0.64 | 0.93 | 0.76 |
| ATRX | 0.56 | 0.85 | 0.33 | 0.48 |
| For HGG | | | | |
| IDH1 | 0.84 | 0.72 | 0.96 | 0.83 |
| Age at diagnosis | 0.74 | 0.67 | 0.68 | 0.67 |
| PTEN | 0.69 | 0.75 | 0.32 | 0.45 |
| EGRF | 0.65 | 0.68 | 0.33 | 0.35 |
| ATRX | 0.56 | 0.48 | 0.91 | 0.63 |

**Table 2**. The computational results of the most informative molecular biomarkers and clinical features for distinguishing between LGGs and HGGs. The performance metrics for each feature, including accuracy, precision, recall, and F1-score, are provided separately for LGGs and HGGs, demonstrating the varying effectiveness of each molecular biomarker and clinical feature in classifying these two tumor types.

feature had the lowest correlation value ($r = 0.24$). The pairwise Pearson's correlation coefficients between the 5 most informative features and glioma tumor grade are shown in Fig. 13.

## Classification performance of classical models

In this study, the performance of the VQC-1 model, which demonstrated the best classification results among the six proposed VQC models, was compared with six different classical ML algorithms using five-fold cross-validation. These classifiers are, K-Nearest Neighbors (KNN), Support Vector Classifier (SVC), Decision Tree Classifier (DTC), Random Forest Classifier (RFC), XGBoost, and Gradient Boosting Machine (GBM). The average accuracy values obtained for these classifiers were determined as 0.82, 0.75, 0.8, 0.82, 0.84 and 0.83, respectively. Detailed results for other evaluation metrics, such as precision, recall, and F1-score, are presented in Supplementary Table 3.

## Discussion

In this section, the results obtained with the ensemble feature selection method and VQC models are discussed in detail. In this context, comparisons are made with studies in the literature. First, the results of the ensemble feature selection process are presented and compared with the findings in the literature. Next, the details and circuit structure of the VQC-1 model, which demonstrated the best classification performance among the six proposed VQC models, are explained. Subsequently, the classification performances of the five most important features in distinguishing LGGs from HGGs are examined, and the molecular and clinical significance of these features is evaluated. Finally, the classification performances of 6 different classical ML models, obtained using 5-fold cross-validation, are analyzed. The 5-fold cross-validation results of the VQC-1 model are compared with both traditional models and similar studies in the literature.

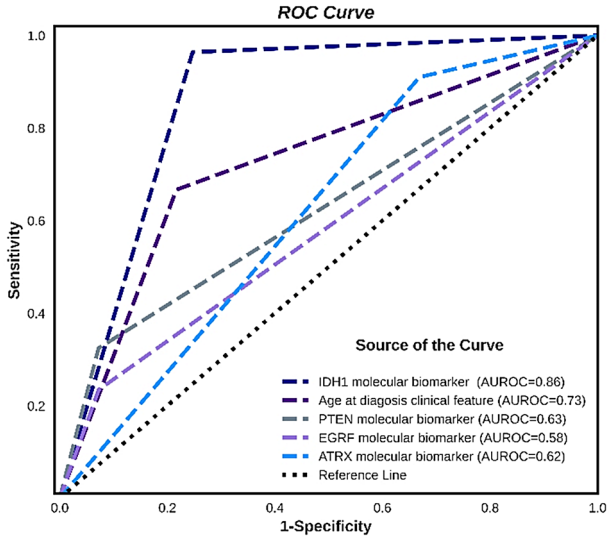



**Fig. 11**. Receiver operating characteristic (ROC) curve analysis for the most informative molecular biomarkers and clinical features in distinguishing LGGs from HGGs. The curve highlights the true positive rate (sensitivity) versus the false positive rate (1-specificity), with IDH1 achieving the highest AUROC value.

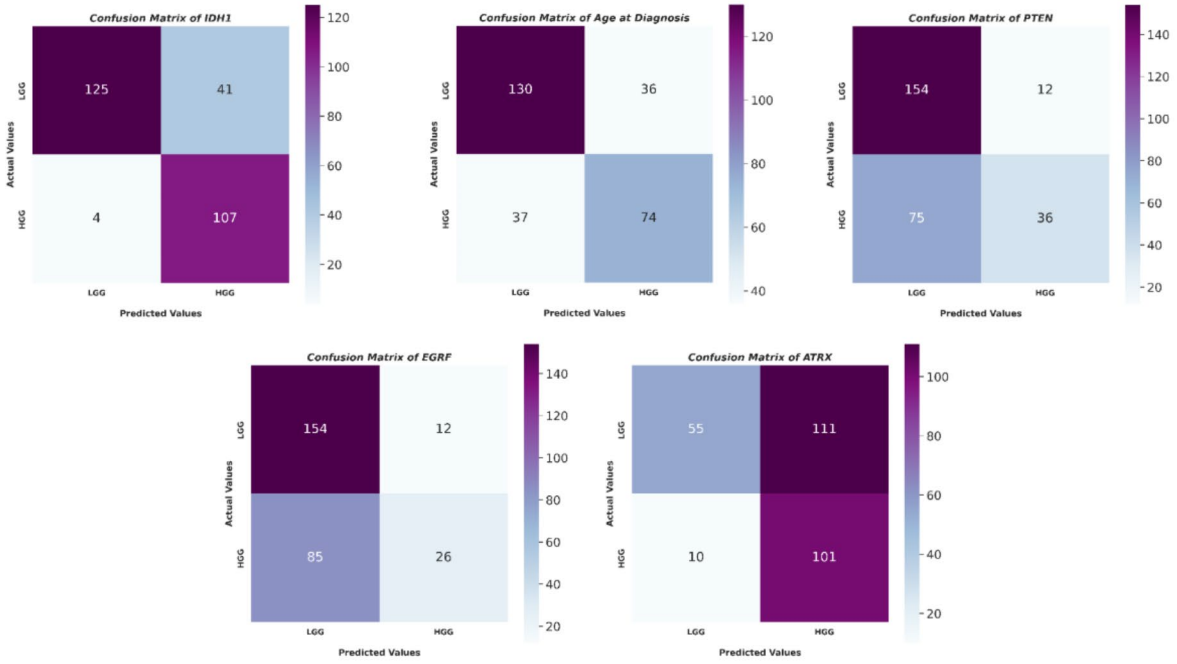



**Fig. 12**. Confusion matrices for the classification performance of individual molecular biomarkers and clinical features in distinguishing LGGs from HGGs. IDH1 and age at diagnosis exhibit the highest predictive power, while ATRX shows the weakest classification capability.

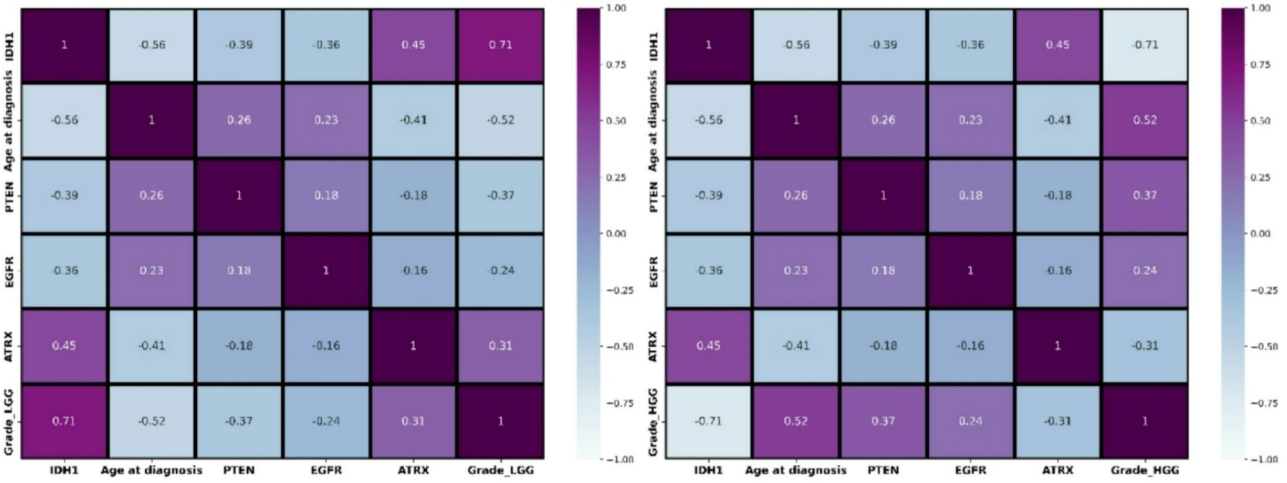



**Fig. 13**. Pairwise Pearson's correlation coefficients between the five most informative molecular marker and clinical features (IDH1, ATRX, PTEN, EGFR, and age at diagnosis) and glioma grade.

## Feature selection

In this section, of the study, the role of the ensemble-based feature selection method is emphasized in the discovery of molecular biomarkers and clinical features for classifying LGGs and HGGs based on TCGA data. As evidenced by numerous studies in the literature[93], many tumors do not arise from a single gene mutation but rather result from a series of genetic alterations. Therefore, the identification of significant molecular biomarkers enables a more accurate correlation of gene expression with disease incidence. Moreover, in the early stages, the identification and selection of significant clinical features alongside these genetic molecular biomarkers are extremely critical in distinguishing between LGGs and HGGs. Additionally, the determination of crucial features significantly impacts the ultimate performance of classifiers. For example, in this study[109], feature selection techniques were used for biomarker discovery in four cancer diagnosis microarray datasets: leukemia, colon, lymphoma, and prostate. To ensure the stability of biomarker identification and enhance classification performance in the subsequent stage, an ensemble feature selection method was proposed. These authors demonstrated that the robustness of support vector machines (SVMs) for biomarker discovery could be significantly increased by employing ensemble feature selection techniques while simultaneously improving classification performance. With the proposed methodology, an increase of almost 0.3 in the robustness of the selected biomarkers, along with an improvement of approximately 0.15 in classification performance, was observed across the 4 microarray datasets. In another study[110], ranking-based feature selection techniques and state-of-the-art feature selection methods were applied to 6 different DNA microarray datasets, namely, Breast, Colon, Leukemia, Lymphoma, Lung, and Ovarian. The effectiveness of these methods was determined using 4 different classifiers. Overall, significant improvements in classification results were observed as the number of features decreased for each dataset compared to using the entire feature set. This demonstrates that the application of feature selection techniques substantially enhances classification performance. Furthermore, in all experiments, it was observed that even without feature selection, the RFC yielded the most favorable outcomes. Identifying the most informative molecular biomarkers and clinical features and finding small feature sets with high classification accuracy is crucial both for minimizing the cost of classification and for biological insight. In many studies, such as[111–113], classical feature selection methods, such as filter, wrapper, and embedded techniques, have been individually emphasized for their positive contributions to classification outcomes. However, there is also a tendency to combine algorithms, as in the case of hybrid, voting-based or ensemble methods, which usually combine two or more feature selection algorithms of different conceptual origins in a sequential manner. Given the complexity and noise in genomic data, obtaining a perfect solution and identifying important features with a single feature selection algorithm can be quite challenging. Therefore, in this article, we used an ensemble feature selection method to evaluate different profiles of the data and to identify informative marker genes and clinical features that facilitate the distinction between LGGs and HGGs. We identified the 5 most significant features by the proposed ensemble-based model: *IDH1*, *age at diagnosis*, *PTEN*, *ATRX*, *and EGRF*. The main reasons for selecting these 5 features are their ability to yield the best classification accuracy, consume less processing time, and require fewer memory configurations than the others. These results are consistent with the findings of previous studies, including various research conducted in the fields of neuroscience and neuro-oncology[26,114–117]. In this study[26], with the aim of enhancing glioma grading performance using TCGA and CGGA glioma datasets, a novel hybrid feature selection method was first proposed. Subsequently, five supervised learning models were employed to investigate the impact of feature selection methods on classification performance. The proposed method, called "GradWise", comprises a rank-based weighted hybrid filter and embedded feature selection techniques aimed at identifying significant molecular markers and clinical features in the TCGA and CGGA glioma datasets. The SVM classifier yielded the most favorable outcomes, achieving an accuracy of 87.007% for the TCGA cohort and 80.412% for the CGGA cohort when utilizing 13 features. For the TCGA dataset, the selected features for the best result included 'CIC', 'Age', 'IDH1', 'PTEN', 'ATRX', 'PIK3R1', 'NF1', 'IDH2',

'GRIN2A', 'NOTCH1', 'TP53', 'EGFR', and 'MUC16'. Moreover, for the CGGA dataset, the best identified features were IDH1, Age, PTEN, PDGFRA, and NF1. The obtained features align with the most informative features identified in our research. In another study[86], a novel hierarchical voting-based methodology was suggested to improve both the identification of significant features and the classification performance of ML models. The methodology created using TCGA and CGGA glioma datasets consists of a combination of voting-based feature selection methods derived from four different feature selection methods (weight of evidence, recursive feature elimination, random forest (RF), LASSO) and the soft voting-based ensemble learning methodology generated from five supervised learning models (LR, SVM, KNN, RF, AdaBoost). The results obtained from the hierarchical voting-based methodology were individually compared with those obtained from the LASSO feature selection method. Consequently, in the TCGA glioma dataset, the highest accuracy of 0.876 was attained through the utilization of SVM, RF, and AdaBoost in combination. On the other hand, for the CGGA glioma dataset, the most favorable accuracy of 0.797 was achieved by employing the combination of SVM, KNN, RF, and AdaBoost.

## Classification performance of VQC models

In this part of the study, by changing the hyperparameters of VQC, such as feature maps, PQC structures and optimization methods, an attempt was made to obtain a circuit design that has minimal quantum gate and circuit depth. The fidelity of modern quantum computation is negatively affected by increasing the number of qubits or gates. Moreover, the training time for quantum circuits can be significantly prolonged by considering phenomena such as barren plateaus[118]. Additionally, the intricacies of designing architectures, selecting optimization functions, and initializing parameters are far more complex and nuanced than one might superficially assume. Therefore, a VQC with optimal hyperparameters not only reduces the training time but also enables us to avoid phenomena such as barren plateaus. In addition, preprocessing steps conducted before the application of VQC significantly improve the classification performance.

For instance, in this study[119], an attempt was made to predict dementia in elderly patients using IBM's VQC model within the Qiskit framework. The performance of this model was compared with that of a classical SVM with a linear kernel considering different numbers of features. In the preprocessing stage before the VQC model, a min–max normalization process was applied, followed by the selection of the most important features. The variable ranking process was carried out based on the scores provided by classifiers using the gradient boosting, RF, extra trees, and K-best ML methods. In the present study, when 3 features related to dementia were utilized, the accuracy of the VQC model approached 0.9, whereas the performance of the SVM with linear kernel model was approximately 0.82. Despite the emphasis on the superiority of the VQC model in the study, no information was provided regarding the gates used within the VQC. In another study[120], the proposed VQC model was applied to solve binary classification problems on a synthetic dataset, as well as real datasets obtained from the University of California Intelligence Machine Learning (UCI), including a sonar dataset and a diabetes dataset. The performance of the suggested VQC model was compared with that of other methods, such as SVM and QSVM. Within the parameterized quantum circuit of VQC, $R_y$, $R_z$ rotational, and CX gates were utilized. To enhance the classification performance, a preprocessing step was introduced. In this step, classical ML methods, namely, RF, LR, and SVM, were employed for feature ranking. Eight important features were identified for each dataset based on these methods. After applying min–max normalization, the features were encoded from the classical space to the quantum Hilbert space using basis and amplitude encoding methods. As a result, the amplitude encoding-based VQC achieved accuracies of 0.984, 0.6730 and 0.7450 on the synthetic, sonar, and diabetes datasets, respectively. This method successfully improved the prediction rates for both the synthetic and diabetes datasets, but its impact on the sonar dataset was limited. In this study[121], a two-stage approach was proposed to classify and subsequently segment brain tumors at the initial stage, aiming to improve patient survival rates. The methodology is designated as Phase 1 and Phase 2 and was tested on three different types of benchmark datasets, namely, TCGA, BRATS 2020, and locally collected images. In Phase 1, the Inceptionv3 model was utilized to extract significant features from brain MR images. The values of the score vectors obtained from the softmax function in the final layer of this pretrained model were employed to classify the brain tumors. These score vectors were then transmitted to a VQC with a 4-qubit structure, for model training. The parametrized circuit included $R_x$, $R_y$, and $R_z$ rotational gates, as well as CX gates. The Kaggle dataset achieved accuracy rates of 0.9944 for no tumor, 0.9925 for meningioma, 0.9803 for pituitary tumors, and 0.9934 for glioma. With respect to classifying tumor and nontumor tumor types, the proposed method achieved an accuracy of 0.9333 on locally collected images. For the 2020-BRATS challenge, the proposed method achieved an accuracy of 0.9091 in differentiating HGGs from LGGs. In Phase 2, to analyze the total infected area postclassification, a modified Seg-Network was introduced, providing global accuracies of 0.982, 0.999, and 0.997 on the Kaggle dataset, locally collected images, and 2020-BRATS Challenge, respectively. Furthermore, in the literature, it has been indicated in numerous studies that hybrid methods enhance the performance of quantum ML techniques. In certain studies, although the performance advantage of the proposed hybrid classical and quantum methods over classical methods is emphasized when applied to problems such as brain tumor classification[122], automatic Alzheimer's diagnosis[123], brain disorder classification[124], and diabetic foot ulcer classification[125], some research has highlighted the advantage of rapid convergence provided by hybrid models, leading to a shortened processing time, even when the performance is equivalent[126].

In our study, after identifying the most informative molecular markers and clinical features through the ensemble feature selection process (as described in "Feature selection", six different VQC models with different hyperparameters were designed using these features. Among these models, the VQC-1 model, which employs $R_x$, rotational and CX gates in the feature map and $R_y$, $R_z$ and CY gates in the parameterized quantum circuit, along with the AQCD optimization method for parameter updates, achieved the highest accuracy in distinguishing between LGGs and HGGs. Here, single-qubit rotational gates ( $R_x$, $R_y$ and $R_z$) are employed to rotate each data qubit in a specific manner for a given class label (LGGs or HGGs), while in two-qubit quantum

gates (CX, CY ) the quantum entanglement phenomenon is leveraged to ensure that the rotation of each data qubit affects all other data qubits in a specified manner, involving them in instantaneous interactions with all possible states of the feature vector. In addition, the features in the TCGA glioma dataset utilized in our study consisted entirely of categorical data, excluding *age at diagnosis*. Quantum state preparation is crucial for establishing a functional flow in a quantum ML model and serves as a significant preprocessing step in VQC. After converting categorical data into a series of binary variables through *one-hot encoding* ("Preprocessing"), $R_x$ rotational and CX gates were employed during the quantum state preparation step.

In addition to these results, before employing the VQC-1 model, we utilized principal component analysis (PCA), which is the most widely used feature extraction method in quantum ML literature. We conducted a performance comparison with our proposed hybrid classical and quantum computing model, demonstrating its impact on the classification results. When PCA was used, the accuracy of the VQC-1 model in distinguishing between LGGs and HGGs was 0.72. Although this accuracy is 0.272 lower than that of our proposed model, many studies in the literature have emphasized the weakness of the PCA method in terms of feature selection[90]. While PCA may provide a speed advantage to quantum ML methods, it renders data interpretation and readability impossible and is not a favorable approach in terms of transparency[90,127]. These findings indicate that our proposed hybrid model not only enhances classification performance but also provides more interpretable results.

## Classification performance of most informative features and correlation analysis between most informative features and glioma tumor grade

Molecular analysis of tumors has significantly impacted the diagnosis and classification of gliomas, yielding substantial implications for both prognosis and treatment guidance. The emergence of DNA methylation studies has provided increased knowledge about specific genetic changes in glioma genomes, facilitating accurate monitoring of glioma patients and paving the way for personalized therapies. Since the inclusion of molecular markers in the WHO classification in 2016 and significant changes in 2021 advancing the role of molecular diagnosis in CNS tumor classification, numerous studies have been conducted to identify crucial molecular markers facilitating the diagnosis and differentiation of glioma tumors. In this section, of our study, we evaluated the performance of the most informative features mentioned in "Feature selection", namely, *IDH1*, *age at diagnosis*, *PTEN*, *ATRX*, *and EGFR*, in differentiating between LGGs and HGGs. The features were tested for their individual predictive values. To assess the performance of each significant feature, the VQC-1 model, as described in "Classification performance of most informative features andcorrelation analysis between most informative features and gliomatumor grade", was employed. Among these five important features, *IDH1* exhibited the highest performance in differentiating between LGGs and HGGs, with an accuracy of 0.84.

As highlighted in numerous recent studies[17,20,128–130], the *IDH1* molecular biomarker has been defined as a significant prognostic factor and molecular diagnostic criterion for investigating the behaviors of LGGs and their subtypes. *IDH1* is an enzyme that catalyzes the oxidative decarboxylation of isocitrate to a-ketoglutarate. This enzyme plays a crucial role in regulating metabolic pathways essential for the normal functions of cells. Approximately 65–90% of LGGs exhibit a mutation in *IDH1*, and this mutation in LGGs results in an increase in genome-wide DNA methylation. The hypermethylated phenotype observed in LGGs with IDH1 mutation has been correlated with an enhanced survival rate. In studies[5,131], it has been emphasized that *IDH1* mutation is almost never found in HGGs, and the commonalities between LGGs without *IDH1* mutation and HGGs have been highlighted in many aspects. These results underscore the significant contribution of the *IDH1* molecular biomarker to the differentiation of LGGs from HGGs. In our study, Pearson's correlation analysis revealed a significant negative correlation ($r = -0.71$, $p < 0.0001$) between the *IDH1* molecular marker and HGG and a strong positive correlation ($r = 0.71$, $p < 0.0001$) between the *IDH1* molecular marker and LGG. The robust negative correlation between the *IDH1* molecular marker and HGGs, as well as the strong positive correlation with LGGs, when well understood and interpreted, can aid in comprehending the genetic differences among tumors. These differences are associated with tumor behavior, prognosis, and treatment response. Indeed, mutations in the *IDH1* gene are acknowledged as clinically significant marker for LGGs and are more frequently found in LGGs than in HGGs[5,131,132]. This finding underscores the utility of the *IDH1* mutation as a crucial indicator in the clinical context, providing valuable insights into the genetic landscape of gliomas and their clinical implications.

The IDH1 molecular marker is followed by the only clinical feature among the five most informative features, namely, *age at diagnosis*, for which the accuracy was 0.74. *Age at diagnosis* is one of the most crucial clinical feature for distinguishing between LGGs and HGGs. LGGs tend to affect younger patients more frequently, with a median age at diagnosis of 44[7]. Numerous studies emphasize that a younger age is often associated with mutational status. On the other hand, the majority of HGGs (approximately 90%) develop de novo in older patients. In many studies in the literature, from clinical information, only *age at diagnosis* has been used for estimating molecular markers[133,134]. For instance, in this study[134], the molecular biomarker IDH and *1p19q codeletion status* were predicted in gliomas using clinical information such as *age*, along with histogram, shape, texture features extracted from preoperative MR images of 538 glioma patients. MRI data obtained from the three institutions were used as the training cohort. The TCGA (for IDH) and TCIA (for 1p19q codeletion status) cohorts were used independently to evaluate the performance of the final model. The RF algorithm was specified as the prediction model with a tree depth of 64 and a maximum of 4096 trees. Additionally, the predictive value of each feature in determining the *IDH* genotype and 1p19q codeletion status was measured using the AUROC. As a result, when *age* and imaging features were used for *IDH* genotype prediction, the model yielded an AUROC of 0.921 in the training cohort and 0.919 in the validation cohort. For *1p19q genotype* prediction, an AUROC of 0.685 was obtained from the training cohort, and 0.716 was obtained from the TCIA test cohort. In both cases, *age* had the highest predictive value. Within our study, Pearson's correlation analysis revealed

a moderate positive correlation ($r = 0.52$, $p < 0.0001$) between the *age at diagnosis* and HGG and a moderate negative correlation ($r = -0.52$, $p < 0.0001$) between the *age at diagnosis* and LGG. These findings demonstrated the significance of *age at diagnosis* in distinguishing between LGGs and HGGs.

*PTEN* is the second molecular marker with the highest accuracy (0.65) among the five most informative features. *PTEN*, or "*Phosphatase and Tensin Homologue*", regulates apoptosis (programmed cell death) and DNA damage repair. In brain tumors, particularly in frontal lobe GBM, there is a decrease in the expression of this gene, and *PTEN* loss is associated with GBM. As indicated in numerous studies, IDH-wildtype GBM (or HGGs) have mutations in the *PTEN* gene. Approximately 40% of GBMs harbor mutations in the *PTEN* gene protein, and approximately 70% exhibit heterozygous loss at the *PTEN* locus. For instance, in this study[135], a clinic-genomic analysis was conducted using data from a total of 1477 glioma patients from TCGA and the Chinese cohort. The results obtained from the univariate survival analysis revealed an association between high-risk glioma patients (HGGs) with shortened survival and deletion of the *PTEN* gene. In our study, Pearson's correlation analysis revealed a weak positive correlation ($r = 0.37$, $p < 0.0001$) between the *PTEN* molecular marker and HGG and a weak negative correlation ($r = -0.37$, $p < 0.0001$) between the *PTEN* molecular marker and LGG. According to these results, although the deletion of the *PTEN* gene is highly important for distinguishing between LGGs and HGGs, it has been demonstrated that this gene is not a sufficient molecular marker for distinguishing LGGs from HGGs.

The *PTEN* molecular marker is followed by the *EGRF* molecular marker, with an accuracy of 0.65 in distinguishing between LGGs and HGGs. *EGRF* or epidermal growth factor receptor (*EGFR*) is, also known as the HER1/ErbB1 receptor, is a molecular marker for determining treatment response and prognosis in gliomas. *EGFR* is a significant activator influencing various signaling pathways and physiological responses, such as proliferation, survival, and tumorigenesis[131]. It is observed in 60% of primary GBMs and is often associated with HGGs[17]. Moreover, the detection of *EGFR* amplification has been indicated as a criterion for the diagnosis of GBM[17]. In some studies, different MRI sequences have been employed for the noninvasive determination of molecular subtypes of GBM, facilitating the detection of *EGFR* and *EGFR* mutations through these sequences[136]. In this study[136], an attempt was made to identify EGFRvIII, the most common variant of *EGFR* and a significant molecular marker for distinguishing the molecular subtypes of GBM, using one of the parameters of magnetic resonance perfusion-weighted imaging, Relative Tumor Blood Volume (rTBV). The ROC curve analysis in the study demonstrated that the rTBV identified EGFRvIII with an accuracy of 0.81. Additionally, it has been indicated that the expression of vascular endothelial growth factor (VEGF) is associated with a higher relative tumor blood volume in patients with GBM. Within our study, Pearson's correlation analysis revealed a weak positive correlation ($r = 0.24$, $p < 0.0001$) between *EGFR* and HGG and a weak negative correlation ($r = -0.24$, $p < 0.0001$) between *EGFR* and LGG.

The fifth and final crucial feature was the *ATRX* molecular marker, which had an accuracy of 0.56 in distinguishing between LGGs and HGGs. *ATRX*, or *alpha-thalassemia/mental retardation X-linked* gene mutation, serves as a robust biomarker that can guide the diagnosis and prognosis of glioma patients. Mutations or losses in the *ATRX* gene are associated with the alternative lengthening of telomeres (ALT) phenotype[41]. This condition significantly influences the biological behaviors of astrocytic tumor cells and is correlated with the survival of patients with astrocytic tumors. Moreover, mutations in this gene are frequently found in LGGs, particularly in nearly 86% of LGGs with *IDH* mutations[5]. Several studies have highlighted the considerable potential of noninvasive methods for predicting *ATRX* in LGGs, offering diagnostic and prognostic insights. For instance, in this study[41], a dataset pertaining to the *ATRX* mutation status of patients in the TCGA database was utilized for *ATRX* prediction in LGGs, with patients from the CGGA cohort serving as an external validation set. After radiomic features were extracted from T2-weighted magnetic resonance images, nine features were selected using the LASSO regression model out of 431 radiomic features. In the final stage, the SVM model was used to predict the *ATRX* mutation status in the training, validation, and external validation sets. As a result, AUC values of 0.94, 0.925, and 0.725 were achieved for each dataset, respectively. Within our study, Pearson's correlation analysis revealed a weak negative correlation ($r = -0.31$, $p < 0.0001$) between the *ATRX* and HGG, as well as a weak positive correlation ($r = 0.31$, $p < 0.0001$) between the *ATRX* and LGG.

In our study, while emphasizing the significance of the *EGFR* and *ATRX* molecular markers, the low correlation values between HGG and LGG grades for these markers (0.24 and −0.24 for *EGFR* and −0.31 and 0.31 for *ATRX*, respectively) can be attributed to several main reasons:

1. Correlation values can be influenced by the complex biological processes underlying gliomas. Molecular markers such as *EGFR* and *ATRX* may not be directly linked to tumor grade, and the observed correlations may be influenced by other factors in these complex processes.
2. Gliomas exhibit significant genetic diversity, and the impact of *EGFR* and *ATRX* mutations on tumor grade may vary among different subtypes. For instance, the *ATRX* biomarker is often used more for distinguishing LGG subtypes than for differentiating between LGGs and HGGs.
3. The size of the dataset used also affects the correlation values. A larger and more diverse dataset could provide a more comprehensive representation of the relationship between *EGFR or ATRX* and glioma grade.
4. The temporal aspects of tumor development and progression may not be fully reflected in static measurements of molecular markers. Changes in the expression of *EGFR* and *ATRX* over time may lead to fluctuations in correlation values with tumor grade.

Finally, although the *IDH1* molecular marker is frequently used alone for distinguishing between LGGs and HGGs, the results obtained in our study suggest that, in addition to *IDH1*, the inclusion of other mutations (*PTEN*, *EGFR*, *and ATRX*) and other clinical information (*age at diagnosis*) may be more beneficial for glioma classification.

## Classification performance of classical models

The performance of the VQC-1 model, which exhibited the best classification results among six different VQC models proposed with various hyperparameters, was compared with six different classical ML algorithms using a five-fold cross-validation method. The classification accuracy values obtained for the classical ML models during this process are as follows: KNN − 0.82, SVC − 0.75, DTC − 0.80, RFC − 0.82, XGBoost − 0.84, and GBM − 0.83. Furthermore, VQC-1 achieved 0.83 accuracy under the same cross-validation setup. These results demonstrate that VQC-1 performs comparably to classical ensemble methods such as XGBoost and GBM, while outperforming KNN, SVC, DTC, and RFC in terms of classification accuracy. These findings indicate that VQC-1 is not only competitive with classical models but also exhibits superior performance in comparison to certain models. This suggests that hybrid classical and quantum computing models may offer promising alternatives for biomedical classification problems. The competitive performance of the proposed hybrid classical and quantum computing model, comparable to classical models, aligns with previous studies showing the effectiveness of ML-based approaches for glioma diagnosis and classification. In the literature, various classical ML models have been used to improve the detection and classification of glioma tumors. For instance, in this study[116], a classification model was developed to identify patients classified as LGG or GBM and to improve clinical decision support processes by considering clinical and molecular/mutational factors using data from The Cancer Genome Atlas (TCGA). The model integrates feature selection methods (Pearson correlation, Mutual Information, and PCA) with various ML-based classification algorithms, including Random Forest, Decision Trees, Logistic Regression, KNN, AdaBoost, SVM, CatBoost, LGBM, and XGBoost, as well as deep learning models (ANN and CNN). An ensemble stacking approach was also employed, and the Final Stack Model demonstrated strong performance. The XGBoost model achieved the highest performance, obtaining 88% accuracy, 82% precision, 94% recall, and 92% AUC. In addition, the Final Stack model achieved 82% accuracy, 79% precision, 85% recall, and 90% AUC. To enhance the model's transparency and clinical applicability, four different explainable artificial intelligence (XAI) techniques (SHAP, LIME, ELI5, and QLattice) were employed. These methods analyzed the decision-making mechanisms of the model and identified the most critical features in glioma diagnosis. The findings indicate that genetic factors such as IDH1, PIK3CA, ATRX, PTEN, CIC, EGFR, TP53, as well as the age at diagnosis, play a crucial role in glioma classification.

Likewise, the study[117] employed the same TCGA dataset to propose a data-centric approach for the accurate prediction and grading of gliomas. To examine the effects of oversampling and limited undersampling algorithms, six ML models (KNN, SVM, multilayer perception—MLP, LR, and two ensemble models, RF and CatBoost) were employed. Additionally, to identify the most informative molecular biomarkers and clinical features, four feature ranking algorithms (information gain, Gini index, chi-square, and random forest) were applied to the normalized data. Using a multiple intersection approach, the most informative features were determined as IDH1, age at diagnosis, PTEN, CIC, and ATRX. Furthermore, the explainability of the predictions was analyzed using global feature importance and SHAP methods, demonstrating that IDH1 and age at diagnosis had the greatest influence on model decisions. As a result, the two ensemble models (RF and CatBoost) exhibited superior performance compared to the other models. Moreover, it was found that the oversampling process applied to the minority class using the SMOTE method improved the predictive performance of the models.

In conclusion, the maximum accuracy obtained when using the five features selected by the ensemble feature selection method (0.74) and the accuracy value obtained through five-fold cross-validation (0.83) indicate that the VQC-1 model demonstrates better generalization when evaluated across multiple training and validation splits. In other words, the model effectively captures all variations within the dataset, exhibiting a more reliable and robust generalization capability. This result suggests that hybrid classical and quantum computing models, due to their strong generalization abilities, may provide more reliable and effective solutions compared to classical models in biomedical applications with complex and highly correlated data, including glioma tumors.

## Conclusions and future works

This paper proposes a novel hybrid classical and quantum computing model to distinguish between LGGs and HGGs. To the best of our knowledge, this study is the first to investigate the differentiation of LGGs from HGGs using the TCGA data within a hybrid classical and quantum computing model. In the classical part of the study, an ensemble model was used to determine the most informative subset of molecular biomarkers and clinical features using the TCGA dataset. The ensemble model combines filter, wrapper, and embedded feature selection methods, utilizing intersection, and multi-intersection methods to determine the most informative features. The most informative features identified by the ensemble model in our study included molecular biomarkers such as *IDH1*, *PTEN*, *EGFR*, *and ATRX* and the clinical feature *age at diagnosis*. The quantum section of our study involved transmitting the most informative features identified by the ensemble model to a quantum learning mechanism for the differentiation of LGGs from HGGs. Within this mechanism, six distinct VQC models with different hyperparameters, including feature maps, parameterized quantum circuits, and optimization methods, are proposed. Among these models, VQC-1, VQC-2, …, and VQC-6, the best classification performance was achieved by the VQC-1 model, which utilizes $R_x$, CX gates in the feature map, $R_y$, $R_z$, and CY gates in the parameterized quantum circuit and employs the AQCD optimization method for parameter optimization. In addition, the ability of each of the 5 most informative features determined by the ensemble feature method to distinguish LGGs from HGGs was determined using VQC-1, according to which *IDH1*, *age at diagnosis*, *PTEN*, *EGFR* and *ATRX* were identified as the most important features that distinguish LGGs from HGGs in descending order of importance. Finally, the classification performance of the VQC-1 model was compared with six different classical ML algorithms using a five-fold cross-validation approach. The findings demonstrate that the VQC-1 model exhibited competitive and effective classification performance compared to classical ML algorithms, achieving consistent results across different data subsets and demonstrating strong generalization capability.

This study demonstrates that hybrid classical and quantum computing models can serve as a powerful alternative to classical models, particularly in the analysis and interpretation of complex and highly correlated biomedical data, such as brain tumors, thereby establishing a significant foundation for future research.

In the future, we aim to apply this method to high-dimensional biomedical imaging data. In addition to the proposed method, we plan to enhance the performance of differentiating LGGs from HGGs by developing new hybrid classical and quantum computing models.

## Data availability

The data in this paper were obtained from The Cancer Genome Atlas (TCGA) Research Network. (https://www.cancer.gov/tcga)

Received: 14 August 2024; Accepted: 2 April 2025
Published online: 17 July 2025

## References

1. Seano, G. (ed) *Brain Tumors* (Springer US, 2021).
2. Ostrom, Q. T. et al. CBTRUS statistical report: primary brain and central nervous system tumors diagnosed in the united States in 2006–2010. *Neuro-Oncology* **15**, ii1–ii56 (2013).
3. Alhasan, A. S. Clinical applications of artificial intelligence, machine learning, and deep learning in the imaging of gliomas: A systematic review. *Cureus*. **13** (2021).
4. Louis, D. N. et al. The 2007 WHO classification of tumours of the central nervous system. *Acta Neuropathol.* **114**, 97–109 (2007).
5. The Cancer Genome Atlas Research Network. Comprehensive, integrative genomic analysis of diffuse lower-grade gliomas. *N. Engl. J. Med.* **372**, 2481–2498 (2015).
6. Wang, Z. et al. Comparative profiling of immune genes improves the prognoses of lower grade gliomas. *Cancer Biol. Med.* **19**, 533–550 (2021).
7. Malmström, A. *Studies for Better Treatment of Patients with Glioma*, vol. 1709 (Linköping University Electronic, 2019).
8. Rajaratnam, V. et al. Glioblastoma: pathogenesis and current status of chemotherapy and other novel treatments. *Cancers* **12**, 937 (2020).
9. C Holland, E. Glioblastoma multiforme: the terminator. *Proc. Natl. Acad. Sci. U. S. A.* **97**, 6242–6244 (2000).
10. Bush, N. A. O., Chang, S. M. & Berger, M. S. Current and future strategies for treatment of glioma. *Neurosurg. Rev.* **40**, 1–14 (2017).
11. Stupp, R. et al. Radiotherapy plus concomitant and adjuvant Temozolomide for glioblastoma. *N. Engl. J. Med.* **352**, 987–996 (2005).
12. Nakada, M. et al. Molecular targets of glioma invasion. *Cell. Mol. Life Sci.* **64**, 458–478 (2007).
13. Pei, L., Jones, K. A., Shboul, Z. A., Chen, J. Y. & Iftekharuddin, K. M. Deep neural network analysis of pathology images with integrated molecular data for enhanced glioma classification and grading. *Front. Oncol.* **11**, 668694 (2021).
14. Zhuge, Y. et al. Automated glioma grading on conventional MRI images using deep convolutional neural networks. *Med. Phys.* **47**, 3044–3053 (2020).
15. Tasci, E. et al. 3D multimodal brain tumor segmentation and grading scheme based on machine, deep, and transfer learning approaches. *Int. J. Bioinform. Intell. Comput.* (2022).
16. Louis, D. N. et al. The 2016 world health organization classification of tumors of the central nervous system: a summary. *Acta Neuropathol.* **131**, 803–820 (2016).
17. Mahajan, A. et al. Glioma radiogenomics and artificial intelligence: road to precision cancer medicine. *Clin. Radiol.* **78**, 137–149 (2023).
18. Chang, P. et al. Deep-learning convolutional neural networks accurately classify genetic mutations in gliomas. *AJNR Am. J. Neuroradiol.* **39**, 1201–1207 (2018).
19. Zhao, Z. et al. Chinese glioma genome atlas (CGGA): A comprehensive resource with functional genomic data from Chinese glioma patients. *Genom. Proteom. Bioinform.* **19**, 1–12 (2021).
20. Kalidindi, N., Or, R., Babak, S. & Mason, W. Molecular classification of diffuse gliomas. *Can. J. Neurol. Sci.* **47**, 464–473 (2020).
21. Louis, D. N. et al. The 2021 WHO classification of tumors of the central nervous system: a summary. *Neuro-Oncology* **23**, 1231–1251 (2021).
22. Ali-Osman, F. (ed) *Brain Tumors* (Humana, 2005).
23. Tomczak, K., Czerwińska, P. & Wiznerowicz, M. Review the cancer genome atlas (TCGA): an immeasurable source of knowledge. *Contemp. Oncol. (Pozn)*. **1A**, 68–77 (2015).
24. Diaz Rosario, M. et al. The next frontier in health disparities—A closer look at exploring sex differences in glioma data and omics analysis, from Bench to Bedside and Back. *Biomolecules*. **12**, 1203 (2022).
25. Tomita, Y. et al. Fifteen-year trends and differences in mortality rates across sex, age, and race/ethnicity in patients with brainstem tumors. *Neuro-Oncol. Adv.* **3**, vdab137 (2021).
26. Tasci, E. et al. A novel application of a rank-based weighted hybrid filter and embedded feature selection method for glioma grading with clinical and molecular characteristics. *Cancers*. **15**, 4628 (2023).
27. DeWitt, J. C. et al. Cost-effectiveness of IDH testing in diffuse gliomas according to the 2016 WHO classification of tumors of the central nervous system recommendations. *Neuro-Oncology* **19**, 1640–1650 (2017).
28. Katsanis, S. H. & Katsanis, N. Molecular genetic testing and the future of clinical genomics. *Nat. Rev. Genet.* **14**, 415–426 (2013).
29. Carter, J. H. et al. Targeted next-generation sequencing in molecular subtyping of lower-grade diffuse gliomas. *J. Mol. Diagn.* **19**, 328–337 (2017).
30. Gutta, S., Acharya, J., Shiroishi, M. S., Hwang, D. & Nayak, K. S. Improved glioma grading using deep convolutional neural networks. *AJNR Am. J. Neuroradiol.* **42**, 233–239 (2021).
31. Tian, Q. et al. Radiomics strategy for glioma grading using texture features from multiparametric MRI. *Magn. Reson. Imaging.* **48**, 1518–1528 (2018).
32. Özcan, H. et al. A comparative study for glioma classification using deep convolutional neural networks. *MBE.* **18**, 1550–1572 (2021).
33. Ertosun, M. G. & Rubin, D. L. Automated grading of gliomas using deep learning in digital pathology images: A modular approach with ensemble of convolutional neural networks. *AMIA Annu. Symp. Proc.* **2015**, 1899–1908 (2015).
34. Sohn, C. K. & Bisdas, S. Diagnostic accuracy of machine learning-based radiomics in grading gliomas: systematic review and meta-analysis. *Contrast Media Mol. Imaging.* **2020**, 1–12 (2020).
35. Banerjee, S., Mitra, S., Masulli, F. & Rovetta, S. Deep radiomics for brain tumor detection and classification from multi-sequence MRI. https://doi.org/10.48550/ARXIV.1903.09240 (2019).

36. Jose, L. et al. Artificial intelligence-assisted classification of gliomas using whole slide images. *Arch. Pathol. Lab. Med.* **147**, 916–924 (2023).
37. Pitarch, C., Ribas, V. & Vellido, A. AI-based glioma grading for a trustworthy diagnosis: an analytical pipeline for improved reliability. *Cancers* **15**, 3369 (2023).
38. Van Der Voort, S. R. et al. Predicting the 1p/19q codeletion status of presumed low-grade glioma with an externally validated machine learning algorithm. *Clin. Cancer Res.* **25**, 7455–7462 (2019).
39. Cao, M. et al. Qualitative and quantitative MRI analysis in IDH1 genotype prediction of lower-grade gliomas: A machine learning approach. *BioMed Res. Int.* **2021**, 1235314 (2021).
40. Kocak, B. et al. Radiogenomics of lower-grade gliomas: machine learning-based MRI texture analysis for predicting 1p/19q codeletion status. *Eur. Radiol.* **30**, 877–886 (2020).
41. Li, Y. et al. Genotype prediction of ATRX mutation in lower-grade gliomas using an MRI radiomics signature. *Eur. Radiol.* **28**, 2960–2968 (2018).
42. Li, Y. et al. MRI features predict p53 status in lower-grade gliomas via a machine-learning approach. *NeuroImage Clin.* **17**, 306–311 (2018).
43. Qian, Z. et al. Radiogenomics of lower-grade gliomas: a radiomic signature as a biological surrogate for survival prediction. *Aging* **10**, 2884–2899 (2018).
44. Fuller, G. N. et al. Molecular classification of human diffuse gliomas by multidimensional scaling analysis of gene expression profiles parallels morphology-based classification, correlates with survival, and reveals clinically-relevant novel glioma subsets. *Brain Pathol.* **12**, 108–116 (2002).
45. Zhou, H. et al. MRI features predict survival and molecular markers in diffuse lower-grade gliomas. *Neuro-Oncology* **19**, 862–870 (2017).
46. Choi, Y. S. et al. Machine learning and radiomic phenotyping of lower grade gliomas: improving survival prediction. *Eur. Radiol.* **30**, 3834–3842 (2020).
47. Flöther, F. F. The state of quantum computing applications in health and medicine. *Res. Dir. Quantum Technol.* 1–21 (2023).
48. Krunic, Z., Flother, F., Seegan, G., Earnest-Noble, N. & Omar, S. Quantum kernels for real-world predictions based on electronic health records. *IEEE Trans. Quantum Eng.* **3**, 1–11 (2022).
49. Ur Rasool, R. et al. Quantum computing for healthcare: A review. *Future Internet*. **15**, 94 (2023).
50. Ciliberto, C. et al. Quantum machine learning: a classical perspective. *Proc. R Soc. A*. **474**, 20170551 (2018).
51. Prousalis, K. & Konofaos, N. A quantum pattern recognition method for improving pairwise sequence alignment. *Sci. Rep.* **9**, 7226 (2019).
52. Boev, A. S. et al. Genome assembly using quantum and quantum-inspired annealing. *Sci. Rep.* **11**, 13183 (2021).
53. Houssein, E. H., Abohashima, Z., Elhoseny, M. & Mohamed, W. M. Hybrid quantum-classical convolutional neural network model for COVID-19 prediction using chest X-ray images. *J. Comput. Des. Eng.* **9**, 343–363 (2022).
54. Amin, J., Anjum, M. A., Gul, N. & Sharif, M. Detection of brain space-occupying lesions using quantum machine learning. *Neural Comput. Appl.* **35**, 19279–19295 (2023).
55. Mishra, N. et al. Breast cancer detection using quantum convolutional neural networks: A demonstration on a quantum computer. *MedRxiv*. https://doi.org/10.1101/2020.06.21.20136655 (2020).
56. Das, R. Quantum machine learning based computer aided diagnosis for skin cancer detection: a statistical performance analysis over classical approach. In *2022 International Conference on Trends in Quantum Computing and Emerging Business Technologies (TQCEBT)* 1–5 (IEEE, 2022).
57. Akpinar, E., Duc, N. M. & KesercI, B. The role of quantum-enhanced support vector machine using multiparametric MRI parameters in differentiating medulloblastoma from ependymoma. In *2022 IEEE International Conference on Quantum Computing and Engineering (QCE)* 882–885 (IEEE, 2022).
58. Akpinar, E. Quantum machine learning in the cognitive domain: Alzheimer's disease study. https://doi.org/10.48550/ARXIV.2401.06697 (2024).
59. Moradi, S. et al. Clinical data classification with noisy intermediate scale quantum computers. *Sci. Rep.* **12**, 1851 (2022).
60. Amin, J., Sharif, M., Gul, N., Kadry, S. & Chakraborty, C. Quantum machine learning architecture for COVID-19 classification based on synthetic data generation using conditional adversarial neural network. *Cogn. Comput.* **14**, 1677–1688 (2022).
61. Ahalya, R. K., Snekhalatha, U. & Dhanraj, V. Automated segmentation and classification of hand thermal images in rheumatoid arthritis using machine learning algorithms: A comparison with quantum machine learning technique. *J. Therm. Biol.* **111**, 103404 (2023).
62. Cao, Y., Romero, J. & Aspuru-Guzik, A. Potential of quantum computing for drug discovery. *IBM J. Res. Dev.* **62** (1–6), 20 (2018).
63. Li, J. et al. Drug discovery approaches using quantum machine learning. https://doi.org/10.48550/ARXIV.2104.00746 (2021).
64. Pyrkov, A. et al. Quantum computing for near-term applications in generative chemistry and drug discovery. *Drug Discov. Today*. **28**, 103675 (2023).
65. Nguyen, N. Biomarker discovery with quantum neural networks: A case-study in CTLA4-Activation pathways. https://doi.org/10.48550/ARXIV.2306.01745 (2023).
66. Preskill, J. Quantum computing in the NISQ era and beyond. *Quantum* **2**, 79 (2018).
67. De Luca, G. Survey of NISQ era hybrid quantum-classical machine learning research. *JAIT* **2**, 9–15 (2021).
68. Cerezo, M. et al. Variational quantum algorithms. *Nat. Rev. Phys.* **3**, 625–644 (2021).
69. Farhi, E., Goldstone, J. & Gutmann, S. A. Quantum approximate optimization algorithm. https://doi.org/10.48550/ARXIV.1411.4028 (2014).
70. Khatri, S. et al. Quantum-assisted quantum compiling. *Quantum* **3**, 140 (2019).
71. Bharti, K. et al. Noisy intermediate-scale quantum (NISQ) algorithms. https://doi.org/10.48550/ARXIV.2101.08448 (2021).
72. Sharma, K., Khatri, S., Cerezo, M. & Coles, P. J. Noise resilience of variational quantum compiling. *New. J. Phys.* **22**, 043006 (2020).
73. Cîrstoiu, C. et al. Variational fast forwarding for quantum simulation beyond the coherence time. *NPJ Quantum Inf.* **6**, 82 (2020).
74. Griol-Barres, I., Milla, S., Cebrián, A., Mansoori, Y. & Millet, J. Variational quantum circuits for machine learning. An application for the detection of weak signals. *Appl. Sci.* **11**, 6427 (2021).
75. Zeguendry, A., Jarir, Z. & Quafafou, M. Quantum machine learning: A review and case studies. *Entropy* **25**, 287 (2023).
76. Majumdar, R., Baral, B., Bhalgamiya, B. & Roy, T. D. Histopathological cancer detection using hybrid quantum computing. https://doi.org/10.48550/ARXIV.2302.04633 (2023).
77. Ray, A., Madan, D., Patil, S., Rapsomaniki, M. A. & Pati, P. Hybrid quantum-classical graph neural networks for tumor classification in digital pathology. *Preprint At.* https://doi.org/10.48550/ARXIV.2310.11353 (2023).
78. T, K., Manikumar, S. S., Dheeraj, T. S. & Sumanth, A. T. Brain tumor recognition based on classical to quantum transfer learning. In *2022 International Conference on Innovative Trends in Information Technology (ICITIIT)* 1–5 (IEEE, 2022).
79. Acar, E. & Yilmaz, İ. COVID-19 detection on IBM quantum computer with classical-quantum transfer learning. *Turk. J. Elec. Eng. Comp. Sci.* **29**, 46–61 (2021).
80. Iyer, V., Ganti, B., Hima Vyshnavi, A. M., Namboori, K., Iyer, S. & P. K. & Hybrid quantum computing based early detection of skin cancer. *J. Interdiscip. Math.* **23**, 347–355 (2020).
81. Nielsen, M. A. & Chuang, I. L. *Quantum Computation and Quantum Information: 10th Anniversary Edition* (Cambridge University Press, 2012).
82. Kaye, P., Laflamme, R. & Mosca, M. *An Introduction to Quantum Computing* (Oxford University Press, 2006).

83. Schumacher, B. Quantum coding. *Phys. Rev. A*. **51**, 2738–2747 (1995).
84. Loredo, R. *Learn Quantum Computing with Python and IBM Quantum Experience: A Hands-on Introduction To Quantum Computing and Writing your Own Quantum Programs with Python* (Packt Publishing, 2020).
85. Gupta, H., Varshney, H., Sharma, T. K., Pachauri, N. & Verma, O. P. Comparative performance analysis of quantum machine learning with deep learning for diabetes prediction. *Complex. Intell. Syst.* **8**, 3073–3087 (2022).
86. Tasci, E., Zhuge, Y., Kaur, H., Camphausen, K. & Krauze, A. V. Hierarchical voting-based feature selection and ensemble learning model scheme for glioma grading with clinical and molecular characteristics. *IJMS*. **23**, 14155 (2022).
87. Yu, L. & Liu, H. Feature selection for high-dimensional data: A fast correlation-based filter solution. In *Proceedings of the 20th International Conference on Machine Learning*. 856–863 (2003).
88. Yilmaz, Ü. & Kuvat, Ö. Investigating the effect of feature selection methods on the success of overall equipment effectiveness prediction. *UUJFE*. 437–452 (2023).
89. Jain, D. & Singh, V. Feature selection and classification systems for chronic disease prediction: A review. *Egypt. Inf. J.* **19**, 179–189 (2018).
90. Remeseiro, B. & Bolón-Canedo, V. A review of feature selection methods in medical applications. *Comput. Biol. Med.* **112**, 103375 (2019).
91. Tadist, K., Najah, S., Nikolov, N. S., Mrabti, F. & Zahi, A. Feature selection methods and genomic big data: a systematic review. *J. Big Data*. **6**, 79 (2019).
92. Venkatesh, B. & Anuradha, J. A. Review of feature selection and its methods. *Cybern. Inform. Technol.* **19**, 3–26 (2019).
93. Liu, B., Cui, Q., Jiang, T. & Ma, S. A combinational feature selection and ensemble neural network method for classification of gene expression data. *BMC Bioinform.* **5**, 136 (2004).
94. Grant, E. et al. Hierarchical quantum classifiers. *NPJ Quantum Inf.* **4**, 65 (2018).
95. Park, G., Huh, J. & Park, D. K. Variational quantum one-class classifier. *Mach. Learn. Sci. Technol.* **4**, 015006 (2023).
96. Lloyd, S., Schuld, M., Ijaz, A., Izaac, J. & Killoran, N. Quantum embeddings for machine learning. *Preprint At.* https://doi.org/10.48550/ARXIV.2001.03622 (2020).
97. Schuld, M. & Killoran, N. Quantum machine learning in feature hilbert spaces. *Phys. Rev. Lett.* **122**, 040504 (2019).
98. Schuld, M. Supervised quantum machine learning models are kernel methods. *Preprint At.* https://doi.org/10.48550/ARXIV.2101.11020 (2021).
99. Wang, Y., Wang, Y., Chen, C., Jiang, R. & Huang, W. Development of variational quantum deep neural networks for image recognition. *Neurocomputing* **501**, 566–582 (2022).
100. Havlíček, V. et al. Supervised learning with quantum-enhanced feature spaces. *Nature* **567**, 209–212 (2019).
101. Benedetti, M., Lloyd, E., Sack, S. & Fiorentini, M. Parameterized quantum circuits as machine learning models. *Quantum Sci. Technol.* **4**, 043001 (2019).
102. Schuld, M. & Petruccione, F. *Machine Learning with Quantum Computers* (Springer International Publishing, 2021).
103. Sim, S., Johnson, P. D. & Aspuru-Guzik, A. Expressibility and entangling capability of parameterized quantum circuits for hybrid quantum-classical algorithms. *Adv. Quantum Tech.* **2**, 1900070 (2019).
104. Ramachandra, A. & Singh, M. A. Hybrid quantum-classical neural network for image classification. (2022).
105. Schuld, M., Bocharov, A., Svore, K. M. & Wiebe, N. Circuit-centric quantum classifiers. *Phys. Rev. A*. **101**, 032308 (2020).
106. Hubregtsen, T., Pichlmeier, J., Stecher, P. & Bertels, K. Evaluation of parameterized quantum circuits: on the relation between classification accuracy, expressibility, and entangling capability. *Quantum Mach. Intell.* **3**, 9 (2021).
107. Koczor, B. & Benjamin, S. C. Quantum analytic descent. *Phys. Rev. Res.* **4**, 023017 (2022).
108. Spall, J. C. An overview of the simultaneous perturbation method for efficient optimization. *Johns. Hopkins Apl Tech. Digest*. **19**, 482–492 (1998).
109. Abeel, T., Helleputte, T., Van De Peer, Y., Dupont, P. & Saeys, Y. Robust biomarker identification for cancer diagnosis with ensemble feature selection methods. *Bioinformatics* **26**, 392–398 (2010).
110. Cilia, N. D., De Stefano, C., Fontanella, F. & Raimondo, S. Scotto Di Freca, A. An experimental comparison of feature-selection and classification methods for microarray datasets. *Information* **10**, 109 (2019).
111. Ebiaredoh-Mienye, S. A., Swart, T. G., Esenogho, E. & Mienye, I. D. A machine learning method with filter-based feature selection for improved prediction of chronic kidney disease. *Bioengineering* **9**, 350 (2022).
112. Chemmakha, M., Habibi, O. & Lazaar, M. Improving machine learning models for malware detection using embedded feature selection method. *IFAC-PapersOnLine* **55**, 771–776 (2022).
113. Tran, C. T., Zhang, M., Andreae, P. & Xue, B. Improving performance for classification with incomplete data using wrapper-based feature selection. *Evol. Intel.* **9**, 81–94 (2016).
114. Siegal, T. Clinical impact of molecular biomarkers in gliomas. *J. Clin. Neurosci.* **22**, 437–444 (2015).
115. Kan, L. K. et al. Potential biomarkers and challenges in glioma diagnosis, therapy and prognosis. *BMJ Neurol. Open.* **2**, e000069 (2020).
116. Palkar, A., Dias, C. C., Chadaga, K. & Sampathila, N. Empowering glioma prognosis with transparent machine learning and interpretative insights using explainable AI. *IEEE Access.* **12**, 31697–31718 (2024).
117. Sánchez-Marqués, R., García, V. & Sánchez, J. S. A data-centric machine learning approach to improve prediction of glioma grades using low-imbalance TCGA data. *Sci. Rep.* **14**, 17195 (2024).
118. McClean, J. R., Boixo, S., Smelyanskiy, V. N., Babbush, R. & Neven, H. Barren plateaus in quantum neural network training landscapes. *Nat. Commun.* **9**, 4812 (2018).
119. Sierra-Sosa, D., Arcila-Moreno, J., Garcia-Zapirain, B., Castillo-Olea, C. & Elmaghraby, A. Dementia prediction applying variational quantum classifier. https://doi.org/10.48550/ARXIV.2007.08653 (2020).
120. Maheshwari, D., Sierra-Sosa, D. & Garcia-Zapirain, B. Variational quantum classifier for binary classification: real vs synthetic dataset. *IEEE Access.* **10**, 3705–3715 (2022).
121. Amin, J. et al. A New Model for Brain Tumor Detection Using Ensemble Transfer Learning and Quantum Variational Classifier. *Comput. Intell. Neurosci.* **2022**, 1–13 (2022).
122. Choudhuri, R. & Halder, A. Brain MRI tumour classification using quantum classical convolutional neural net architecture. *Neural Comput. Appl.* **35**, 4467–4478 (2023).
123. Shahwar, T. et al. Automated detection of Alzheimer's via hybrid classical quantum neural networks. *Electronics* **11**, 721 (2022).
124. Alsharabi, N., Shahwar, T., Rehman, A. U. & Alharbi, Y. Implementing magnetic resonance imaging brain disorder classification via AlexNet–Quantum learning. *Mathematics* **11**, 376 (2023).
125. Alavi, A. & Akhoundi, H. Hybrid classical-quantum method for diabetic foot ulcer classification. https://doi.org/10.48550/ARXIV.2110.02222 (2021).
126. Ajlouni, N., Özyavaş, A., Takaoğlu, M., Takaoğlu, F. & Ajlouni, F. Medical image diagnosis based on adaptive hybrid quantum CNN. *BMC Med. Imaging*. **23**, 126 (2023).
127. Sierra-Sosa, D., Arcila-Moreno, D., Garcia-Zapirain, J., Elmaghraby, A. & B. & Diabetes type 2: poincaré data preprocessing for quantum machine learning. *Comput. Mater. Continua*. **67**, 1849–1861 (2021).
128. Mirchia, K., Richardson, T. E. & Beyond IDH-Mutation: emerging molecular diagnostic and prognostic features in adult diffuse gliomas. *Cancers* **12**, 1817 (2020).
129. Han, S. et al. IDH mutation in glioma: molecular mechanisms and potential therapeutic targets. *Br. J. Cancer*. **122**, 1580–1589 (2020).

130. Appin, C. L. & Brat, D. J. Molecular genetics of gliomas. *Cancer J.* **20**, 66–72 (2014).
131. Ludwig, K. & Kornblum, H. I. Molecular markers in glioma. *J. Neurooncol.* **134**, 505–512 (2017).
132. Huse, J. T. & Aldape, K. D. The evolving role of molecular markers in the diagnosis and management of diffuse glioma. *Clin. Cancer Res.* **20**, 5601–5611 (2014).
133. Batchala, P. et al. Neuroimaging-Based classification algorithm for predicting 1p/19q-Codeletion status in IDH-Mutant lower grade gliomas. *Am. J. Neuroradiol.* **40**, 426–432 (2019).
134. Zhou, H. et al. Machine learning reveals multimodal MRI patterns predictive of isocitrate dehydrogenase and 1p/19q status in diffuse low- and high-grade gliomas. *J. Neurooncol.* **142**, 299–307 (2019).
135. Zhang, B. et al. A prognostic risk model for glioma patients by systematic evaluation of genomic variations. *iScience* **25**, 105681 (2022).
136. Tykocinski, E. S. et al. Use of magnetic perfusion-weighted imaging to determine epidermal growth factor receptor variant III expression in glioblastoma. *Neuro-Oncology* **14**, 613–623 (2012).

## Acknowledgements

The authors would like to acknowledge that this paper is submitted in partial fulfillment of the requirements for PhD degree at Yildiz Technical University.This work was supported by the Research Fund of Yildiz Technical University. Project Number: 5936. This research used resources of the National Energy Research Scientific Computing Center, a DOE Office of Science User Facility supported by the Office of Science of the U.S. Department of Energy under Contract No. DE-AC02-05CH11231 using NERSC award NERSC DDR-ERCAP0033396.

## Author contributions

E.A: Coding, data analysis and interpretation, writing of the paper, design of the study, revision of the scientific content of the manuscript, final approval of the version to be submitted. M.O: Supervising the research and final approval of the version to be submitted.

## Declarations

## Competing interests

The authors declare no competing interests.

## Ethical statement

Since the patients had been anonymized in advance by TCGA and their pertinent data were accessible for public retrieval, our study did not necessitate approval from an institutional review board or adherence to the Health Insurance Portability and Accountability Act.

## Additional information

**Supplementary Information** The online version contains supplementary material available at https://doi.org/10.1038/s41598-025-97067-3.

**Correspondence** and requests for materials should be addressed to E.A.

**Reprints and permissions information** is available at www.nature.com/reprints.

**Publisher's note** Springer Nature remains neutral with regard to jurisdictional claims in published maps and institutional affiliations.

**Open Access** This article is licensed under a Creative Commons Attribution-NonCommercial-NoDerivatives 4.0 International License, which permits any non-commercial use, sharing, distribution and reproduction in any medium or format, as long as you give appropriate credit to the original author(s) and the source, provide a link to the Creative Commons licence, and indicate if you modified the licensed material. You do not have permission under this licence to share adapted material derived from this article or parts of it. The images or other third party material in this article are included in the article's Creative Commons licence, unless indicated otherwise in a credit line to the material. If material is not included in the article's Creative Commons licence and your intended use is not permitted by statutory regulation or exceeds the permitted use, you will need to obtain permission directly from the copyright holder. To view a copy of this licence, visit http://creativecommons.org/licenses/by-nc-nd/4.0/.

© The Author(s) 2025